Contents lists available at ScienceDirect

Arabian Journal of Chemistry

journal homepage: www.ksu.edu.sa

Identification of structural and optical properties and adsorption performance of $(Cd_{0.4}Ni_{0.4}Mn_{0.2})Fe_{2-x}Ru_xO_4$ nanoparticles for the removal of Congo red dye

Serine Kassem [a], Nour AlHajjar [a], Amani Aridi [b,c,*], Ramadan Awad [d]

[a] Physics Department, Faculty of Science, Beirut Arab University, Beirut, Lebanon
[b] Chemistry Department, Faculty of Science, Beirut Arab University, Beirut, Lebanon
[c] Inorganic and Organometallic Coordination Chemistry Laboratory, Faculty of Sciences I, Lebanese University, Hadath, Lebanon
[d] Physics Department, Faculty of Science, Alexandria University, Alexandria, Egypt

ARTICLE INFO

Keywords:
$(Cd_{0.4}Ni_{0.4}Mn_{0.2})Fe_{2-x}Ru_xO_4$ nanoferrite
Adsorption
Congo red removal
Adsorption kinetics
Adsorption isotherm

ABSTRACT

In the field of industrial wastewater treatment, the application of highly efficient methods such as adsorption is crucial for effectively eliminating dangerous pollutants before effluent discharge. Ferrite nanoparticles (NPs) have emerged as promising candidates for the efficient and sustainable removal of dyes from wastewater. Therefore, the synthesis, characterization, and application of $(Cd_{0.4}Ni_{0.4}Mn_{0.2})Fe_{2-x}Ru_xO_4$ ($0 \leq x \leq 0.04$) NPs as adsorbents for the removal of Congo Red (CR) dye, is reported in this study. The X-ray powder diffraction (XRD) analysis has confirmed the purity of the samples with a very small amount of hematite phase. The prepared NPs have pseudo-spherical morphology and average particle size in the range of 12–17 nm. Furthermore, the elemental compositions, estimated from the energy dispersive x-ray (EDX) measurements, indicate the homogenous distribution of elements and the substitution of the Fe^{3+} host ions by the Ru^{3+} dopant. As the Ru content increases from 0.00 to 0.04, S_{BET} increases from 52.39 to 78.34 m^2/g, respectively. Furthermore, the pore diameter, ranging between 12.71 and 18.38 nm, reveals the mesoporous nature of the prepared samples. The direct and indirect bandgap energy, calculated from UV–vis spectroscopy analysis, is in the range of 3.049–3.232 eV and 1.894–2.642 eV, respectively. The adsorption performance of the prepared NPs for the removal of CR dye solution was investigated by varying the contact time, adsorbent amount, pH, and reaction temperature. The adsorption process follows a second-order kinetic model and the NPs with $x = 0.015$ revealed the highest adsorption rate with a rate constant $k_2 = 2.7 \times 10^{-3}$ $g.mg^{-1}.min^{-1}$. The optimum experimental conditions, achieved in the presence of 80 mg of $(Cd_{0.4}Ni_{0.4}Mn_{0.2})Fe_{1.985}Ru_{0.015}O_4$ NPs at 308 K and in the acidic medium at pH = 3.45, result in the removal of 87.5 % of CR dye after 60 min. After applying several non-linear adsorption isotherm models, mainly Langmuir, Freundlich, and Temkin isotherms, the experimental data were well-fitted with the Temkin isotherm model. The strong interactive force between CR and $(Cd_{0.4}Ni_{0.4}Mn_{0.2})Fe_{1.985}Ru_{0.015}O_4$ nanoparticles is revealed from the high value of b_T knowing that $b_T = 182.91$ $J.mol^{-1}$.

1. Introduction

Nanoparticles (NPs) are defined as materials with dimensions ranging from 1 to 100 nm, ensuring at least one dimension falls within this range (Phan & Haes, 2019). The size and shape of nanomaterials play a crucial role in determining their physical and chemical properties (Mathew & Juang, 2007; Phan & Haes, 2019). Thus, scientists are dedicating significant efforts towards the fabrication and the precise control of nanomaterials' morphology and size (Ahmad et al., 2022; Mathew & Juang, 2007). Moreover, the unique combination of magnetic properties, tunability, stability, and multi-functionality makes ferrite NPs stand out among other nanoparticles, offering significant potential for various technological and biomedical applications (Hammad, 2022). Researchers have utilized ferrite nanoparticles in the removal of dyes and organic pollutants which are recognized as significant sources of pollution (Aljohani et al., 2023). Among several wastewater treatment methods, adsorption is considered the most effective method (Alrefaee et al., 2023; Zafar et al., 2022). It is widely used in several studies due to

---

* Corresponding author at: Chemistry Department, Faculty of Science, Beirut Arab University, Beirut, Lebanon.
E-mail address: a.aridi@bau.edu.lb (A. Aridi).

https://doi.org/10.1016/j.arabjc.2023.105477
Received 18 July 2023; Accepted 22 November 2023

its simplicity, cost-effectiveness, and low secondary waste production (Almahri et al., 2023; Bashir et al., 2023; Bazrafshan et al., 2021). It is worth mentioning that the use of nanomaterials in the field of adsorption has garnered significant attention. This interest stems from their small particle size and high surface area (Ghamkhari et al., 2020).

According to the crystal structure and the chemical compositions, ferrites are divided into three different types: spinel, garnets, and hexaferrites (Mathew & Juang, 2007; Sarveena, 2021). The current research will shed light on the spinel ferrites nanoparticles that fall under the category of ceramic substances, composed of iron oxide blended with other metals adopting the general $A^{2+}Fe^{3+}Fe_2O_4$ formula (Bajorek et al., 2019). It is of significance that A represents a divalent cation such as nickel, zinc, barium, cadmium, cobalt, or manganese. Spinel ferrites find extensive applications in the fields of electronics, industry, and biomedicine. They are utilized in various areas such as permanent magnets, telecommunications devices, wastewater treatment, targeted drug delivery, cancer treatment, and magnetic resonance imaging (MRI) (Bajorek et al., 2019; Kefeni et al., 2020; Kefeni & Mamba, 2020). Generally, spinel ferrites nanoparticles may exhibit normal spinel structure, such as $ZnFe_2O_4$ and $CdFe_2O_4$, where all A^{2+} and the Fe^{3+} cations occupy the tetrahedral (A) sites and the octahedral (B) sites, respectively (Sarveena, 2021). Whereas in inverse spinel structure, A^{2+} ions occupy the octahedral sites while Fe^{3+} ions are distributed over both octahedral and tetrahedral sites and this can be found in $NiFe_2O_4$, $CoFe_2O_4$, and $MgFe_2O_4$ (Sarveena, 2021). In mixed spinel structure, both A^{2+} and Fe^{3+} ions are distributed over the tetrahedral and the octahedral sites (Sarveena, 2021). $MnFe_2O_4$ is an example of a material exhibiting a mixed spinel structure. The arrangement of Mn^{2+} and Fe^{3+} creates a unique crystal structure with distinctive properties, making $MnFe_2O_4$ suitable for various applications, including magnetic, electrical, and catalytic applications (Akhlaghi & Najafpour-Darzi, 2021; A. Kumar et al., 2023).

Recently, there has been significant attention focused on tri-metal ferrite NPs among the various investigated spinel ferrites. For instance, $Ni_{0.5}Zn_{0.5}Bi_{0.04}Nd_xFe_{1.96-x}O_4$ has been synthesized by the citrate precursor technique. The current–voltage variation showed a high order of resistivity that is useful in high-frequency applications (Taneja et al., 2022). Furthermore, $Ni_{0.4}Cu_{0.3}Zn_{0.3}Fe_2O_4$ doped with additive Nb_2O_5 showed varied structural properties and yielded soft ferrite entities with tailored magnetic and optical parameters (Patil et al., 2022). Moreover, $Ni_{0.7}Mn_{0.2}Cu_{0.1}Fe_{2-x}Al_xO_4$ nanoferrites were synthesized by sol–gel auto-combustion technique at room temperature. The prepared ferrites exhibited excellent crystal structure, enhanced initial permeability, and good strain size (Suresh et al., 2022). It is worth noting that these ferrite NPs can be synthesized using several methods, and the co-precipitation technique is the best one due to its possibility of controlling the size of the NPs and cost-effectiveness (Bazrafshan et al., 2023).

Studying the properties of cadmium-nickel-manganese ferrite NPs is highly interesting due to the diverse properties exhibited by each of $CdFe_2O_4$, $NiFe_2O_4$ and $MnFe_2O_4$ NPs. For example, in a previous investigation, $CdFe_2O_4$ was used as an effective adsorbent for the removal of Methylene Blue from an aqueous solution, and the removal percentage obtained was over 99 % (Vodă et al., 2016). Moreover, $Ni_{(1-x)}Mn_xFe_2O_4$ exhibited effective performance for the removal of Congo red dye (Luo et al., 2018). In addition, nickel ferrite nanocomposites were prepared using chemical co-precipitation and applied for efficient removal of phenol from the aqueous solutions by adsorption process, and more than 96 % of phenol was removed (Mohammadi et al., 2021). Furthermore, $MnFe_2O_4$ was used as an efficient adsorbent in the removal of Acid Red B dye from water (Wu & Qu, 2005).

Numerous investigations have been conducted to explore the characteristics of pure $CdFe_2O_4$, $NiFe_2O_4$, and $MnFe_2O_4$ nanoparticles. However, there is a noticeable gap in the existing literature concerning the properties of tri-metal ferrite nanoparticles. To address this gap, our study introduces a novel approach by synthesizing tri-metal ferrite nanoparticles known as Cd-Ni-Mn ferrite nanoparticles to enhance their properties. It is worth noting that this particular tri-metal ferrite nanoparticle has not been synthesized or studied previously. Additionally, by incorporating ruthenium (Ru) into the crystal structure, the properties of the resulting ferrite material can be further modified and tailored (Manikandan et al., 2019). Thus, this work reports the synthesis and characterization of $(Cd_{0.4}Ni_{0.4}Mn_{0.2})Fe_{2-x}Ru_xO_4$ ($0.00 \le x \le 0.04$) NPs. Furthermore, the effect of Ru dopant content on the structural and optical properties of $(Cd_{0.4}Ni_{0.4}Mn_{0.2})Fe_{2-x}Ru_xO_4$ NPs was investigated. Besides, the adsorption performance of the prepared NPs for the removal of CR dye was studied.

2. Experimental techniques

2.1. Synthesis of $(Cd_{0.4}Ni_{0.4}Mn_{0.2})Fe_{2-x}Ru_xO_4$ NPs

$(Cd_{0.4}Ni_{0.4}Mn_{0.2})Fe_{2-x}Ru_xO_4$ NPs, where x = 0.00, 0.005, 0.01, 0.015, 0.02 and 0.04, were prepared via the coprecipitation method. The preparation involved the use of high-purity salt chloride precursors, including cadmium (II) chloride hemipentahydrate, nickel (II) chloride hexahydrate, manganese (II) chloride tetrahydrate, ruthenium (III) chloride hydrate and iron (III) chloride hexahydrate. The appropriate stoichiometric proportions of the salt chlorides were dissolved in deionized water to form cationic solutions. Then, the prepared cationic solutions were mixed and stirred for 30 min to improve the homogeneity of the solutions. After that, 4 M NaOH solution was added dropwise to obtain a solution with a pH value of 12. Then, the obtained mixture was heated at 80 °C for 2 h accompanied by continuous stirring. Afterward, a mixture of ethanol and deionized water was used to wash the precipitates until the pH of the filtrate solution dropped to 7. The precipitates were dried in the oven at 100 °C for 18 h. Lastly, grinding and the calcination of the NPs were carried out at 600 °C for 5 h (Aridi et al., 2021; Chehade et al., 2022).

2.2. Characterization of $(Cd_{0.4}Ni_{0.4}Mn_{0.2})Fe_{2-x}Ru_xO_4$ NPs

The crystallinity, crystal structure, and phase purity of the synthesized NPs were examined by XRD using Bruker D8 Focus powder diffractometer with Cu-K_α radiation ($\lambda = 1.5406$ Å) where the diffraction angle 2θ ranges between 20° and 80°. The JEM-2100 was used for the TEM analysis to record the morphology and particle size distribution. To perform the EDX and SEM techniques, the JOEL scanning electron microscope (JSM-5300) was used. The textural properties were evaluated using the N_2 adsorption–desorption method via a 650 Full ISO therme physisorption analyzer. Moreover, the optical properties of the prepared NPs were determined using a JASCO V-670 spectrophotometer at room temperature in the range of 200–700 nm (Aridi et al., 2021).

2.3. Adsorption performance of $(Cd_{0.4}Ni_{0.4}Mn_{0.2})Fe_{2-x}Ru_xO_4$ NPs

The adsorption performance of $(Cd_{0.4}Ni_{0.4}Mn_{0.2})Fe_{2-x}Ru_xO_4$ NPs, where $0.00 \le x \le 0.04$, was evaluated for the removal of CR dye. All adsorption tests are performed in the dark. To identify the sample with the best adsorption activity, 60 mg of each sample was mixed with 150 mL of 30 ppm CR dye solution. At a specified time interval, 3 mL was extracted from the reaction mixture and analyzed using a UV–vis spectrophotometer (Jasco V-650) to measure the remaining concentration of CR dye in the solution. The adsorbed quantity (q_e) of CR was calculated using the following equation (Samoila et al., 2015):

$$qe = \frac{(C_0 - C_e) \times V}{m} \tag{1}$$

where C_0 (mg.L^{-1}) and C_e (mg.L^{-1}) denote the initial CR dye concentration and the dye concentration at equilibrium, respectively, V (L) is the volume of the CR solution, and m (g) is the mass of the adsorbent.

The sample that displayed the most efficient adsorption performance and exhibited the highest rate constant was selected for a comprehensive study to assess the impact of various factors on the adsorption rate. These factors included contact time, adsorbent amount (20, 40, 60, 80, and 100 mg), pH level (2.99, 3.45, 4.19, 7.46, 9.85, and 11.01), and temperature (303, 308, 313, 318 and 323 K) to investigate their influence on the adsorption reaction rate. It is important to note that the pH of the CR solution was adjusted by adding a few drops of 0.1 M HCl and NaOH. After conducting the adsorption reaction at various temperatures, the thermodynamic parameters were calculated, such as the change in the enthalpy (ΔH^0), the change in the entropy (ΔS^0) and the change in the Gibbs free energy (ΔG^0). Subsequently, different adsorption isotherms mainly Langmuir, Freundlich, and Temkin isotherms, to determine the model that best fits the experimental data. It is worth noting that the adsorption experiments were conducted three times to ensure accuracy and reliability.

3. Results and discussion

3.1. XRD analysis

XRD was performed to determine the structure, crystallite size, and lattice parameter of synthesized NPs. The fitting of the XRD patterns of $(Cd_{0.4}Ni_{0.4}Mn_{0.2})Fe_{2-x}Ru_xO_4$ NPs, represented in Fig. 1 (a), was performed by Rietveld refinement using the MAUD software. Major diffraction peaks are located at 2θ ≈ 29.8°, 35.1°, 42.7°, 52.9°, 56.4°, 61.9°, 69.9°, and 73.2°, corresponding to the (220), (311), (400), (422), (511), (440), (620) and (533) planes, respectively. This confirms the formation of the spinel cubic structure, with space group Fd3m (Basma et al., 2022). The refined structure of pure $(Cd_{0.4}Ni_{0.4}Mn_{0.2})Fe_2O_4$ NPs, obtained from the Visualization of Electronics and Structural Analysis (VESTA) software, is shown in Fig. 1 (b). Furthermore, the extracted parameters from Rietveld refinement are listed in Table 1. The weighted profile R-factor (R_{wp}) and the expected R-factor (R_p) are approximately equal and the goodness of fit (χ^2~ 1). Thus, the fitting is reliable and the patterns are well-refined. It is clear that a small fraction of the hematite phase (1.51 %) appears in the pure NPs. However, upon doping NPs with Ru^{3+} dopant, the percentage of hematite phases is reduced to 0.48 % for NPs with x = 0.04. This means that the dopants' ions are successfully incorporated with the spinel ferrite without altering the crystal structure or producing a secondary phase. This result is comparable with a previous study that analyzed the XRD data of $Ni_{0.7}Zn_{0.3}Er_xFe_{2-x}O_4$ NPs, and the intensity of the hematite phase decreased with the increasing of Er content (Sandeep et al., 2022).

The lattice parameter *a*, listed in Table 1, was extracted from MAUD software and determined from Bragg's Law as well. Both methods reveal the same trend. It's observed that the lattice parameter increases from 8.462 to 8.482 Å as the Ru content (x) increases from 0.00 to 0.04. This increase is mainly attributed to the doping of NPs with Ru^{3+} ions having greater ionic radii (0.68 Å) compared to the ionic radii Fe^{3+} (0.65 Å) (Vinod et al., 2022). The values lattice parameter *a* followed an unsystematic variation with the increase of Ru content. As Ru content increases, the Ru^{3+} ions do not easily occupy their positions at A or B sublattice sites therefore some of the ions will be located at grain boundaries (Vinod et al., 2022). The X-ray density ρ, listed in Table 1, was determined using the following equation (Singh Yadav et al., 2018):

$$\rho = \frac{8M}{N_a a^3} \tag{2}$$

where N_a is the Avogadro number, M is the molecular weight, and a is the lattice parameter. It's obviously shown that the X-ray density is inversely proportional to the lattice parameter. The variation in the X-ray density might be attributed to the unremarkable variation between

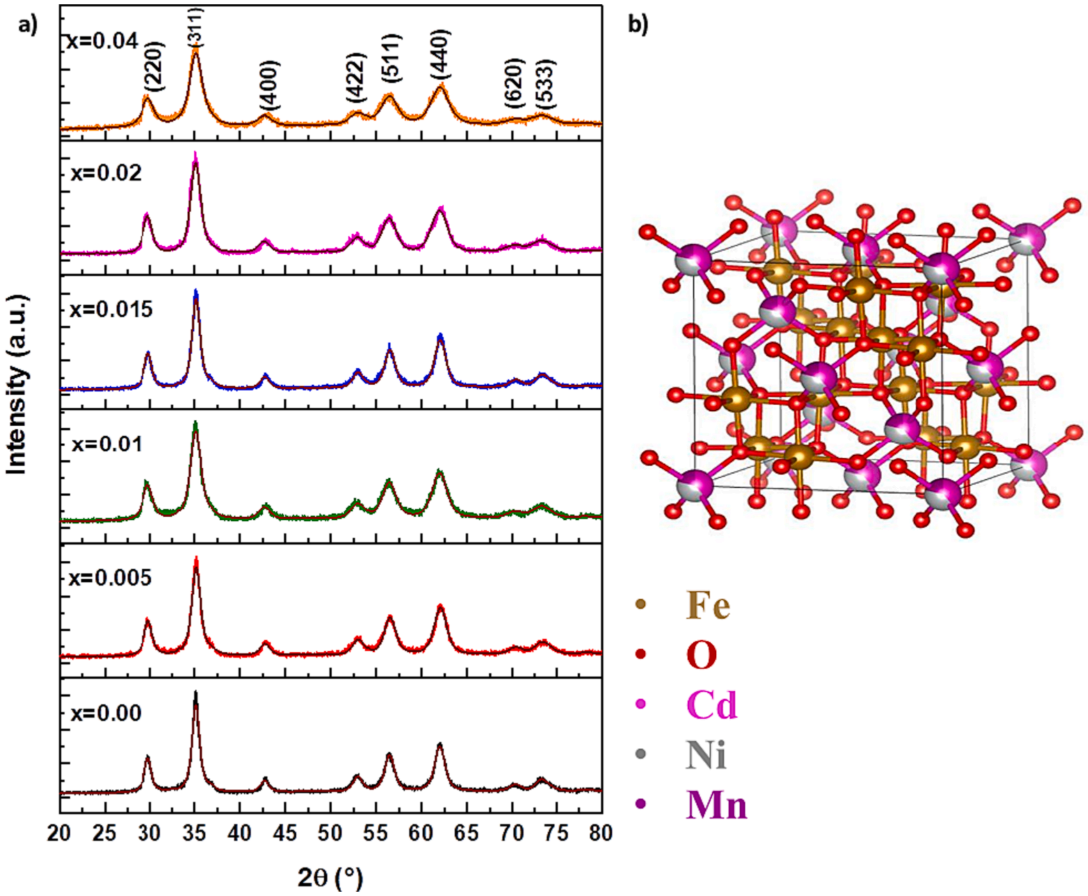

Fig. 1. (a) XRD patterns of $(Cd_{0.4}Ni_{0.4}Mn_{0.2})Fe_{2-x}Ru_xO_4$ NPs where 0.00 ≤ x ≤ 0.04 and (b) refined structure of pure $(Cd_{0.4}Ni_{0.4}Mn_{0.2})Fe_2O_4$ NPs.

Table 1

Extracted parameters from Rietveld refinements of $(Cd_{0.4}Ni_{0.4}Mn_{0.2})Fe_{2-x}Ru_xO_4$ nanoparticles using MAUD software.

Ru content	***x***	0.00	0.005	0.01	0.015	0.02	0.04
Phase percentage %	$\mathbf{(Cd_{0.4}Ni_{0.4}Mn_{0.2})Fe_{2-x}Ru_xO_4}$	98.48	98.73	99.05	99.21	99.44	99.51
	$\mathbf{Fe_2O_3}$	1.51	1.26	0.94	0.78	0.55	0.48
R_{wp}		0.099	0.1	0.1	0.1	0.1	0.1
R_{exp}		0.08	0.08	0.079	0.08	0.08	0.08
χ^2		1.23	1.24	1.27	1.28	1.38	1.28
Lattice parameter Å	***a* MAUD**	8.462	8.454	8.467	8.455	8.469	8.482
	***a* Bragg's law**	8.472	8.471	8.489	8.469	8.490	8.492
***M* g/mol**		255.115	255.341	255.567	255.793	256.019	256.924
ρ **g/cm^3**		5.592	5.613	5.593	5.620	5.599	5.591

the lattice parameter and M (Basma et al., 2022).

To determine the crystallite size of the prepared NPs, the XRD profile analysis was carried out using three different methods, the Debye-Scherrer Model (D-S), the Uniform Deformation Model (UDM) from the Williamson-Hall approach, and the size-strain plot (SSP), the obtained results are listed in Table 2. In the first method the crystallite size $D_{D\text{-}S}$ was calculated from the broadening of XRD peaks using the Debye-Scherrer formula for the Lorentzian peak (Kumar et al., 2015):

$$\mathrm{D}_{D-S} = \frac{0.9\,\lambda}{\beta\cos\theta} \tag{3}$$

by which, β denotes the full width at half maximum (FWHM), λ is the X-ray wavelength (1.5406 Å), and 2θ is the angle of diffraction. The second method was calculating the D_{UDM} via the UDM from the Williamson-Hall method by applying the following equation (Chellab & Harbbi, 2019):

$$\beta\cos\theta = \left(\frac{k\lambda}{D_{UDM}}\right) + (4\varepsilon\sin\theta), \tag{4}$$

where k is a dimensionless shape factor, with a value close to unity and ε is the lattice strain. The practical application of this method involves plotting βcosθ against 4sinθ, knowing that the lattice strain ε and D_{UDM} are estimated from the slope and intercept, respectively (Chellab & Harbbi, 2019). The third method, used to calculate D_{SSP}, is the Size-Strain plot method as represented in the following equation (Chellab & Harbbi, 2019):

$$(d_{hkl}\beta\cos\theta)^2 = (\frac{k}{D_{SSP}})(d_{hkl}^2\beta\cos\theta) + (\frac{\varepsilon}{2})^2, \tag{5}$$

The change in the values of the crystallite size, in the three methods, is due to the substitution of Ru^{3+} ions for Fe^{3+} ions on the lattice sites. By which, the ionic radii of Ru^{3+} ion (0.68 Å) is large as compared to Fe^{3+} ion (0.645 Å). So, it's not easy to replace Fe^{3+} ions on the lattice site, and thus some of the Ru^{3+} ions may reside on the grain boundaries (Thakur et al., 2016).

The crystallite size determined from UDM and SSP models follows the same trend with increasing the Ru content. However, the high values of the coefficient of determination R^2 obtained from the SSP method ensure the well-fitting and reliability of this method. Thus, SSP is the best method for determining the crystallite size of the prepared NPs.

Table 2

Crystallite size, strain, and R^2 values of $(Cd_{0.4}Ni_{0.4}Mn_{0.2})Fe_{2-x}Ru_xO_4$ NPs determined by Debye-Scherrer ($D_{D\text{-}S}$), Uniform Deformation Model (D_{UDM}), and size-strain plot (D_{SSP}) Models.

x	**0.00**	**0.005**	**0.01**	**0.015**	**0.02**	**0.04**
$D_{D\text{-}S}$ **nm**	8.861	6.017	5.411	8.130	6.036	5.520
D_{UDM} **nm**	21.331	18.243	14.148	14.005	19.528	20.094
Strain UDM	0.0065	0.0096	0.0089	0.0049	0.0092	0.0132
R^2 **UDM**	0.9115	0.9054	0.6483	0.8404	0.6596	0.9586
D_{SSP} **nm**	14.754	10.588	10.112	9.890	10.344	17.647
Strain SSP	0.0022	0.0031	0.0035	0.0015	0.0027	0.0045
R^2 **SSP**	0.9351	0.9092	0.8646	0.9774	0.7861	0.9015

3.2. TEM, HRTEM and SAED analysis

Fig. 2 displays the TEM images and histograms, representing the particle size distribution, of $(Cd_{0.4}Ni_{0.4}Mn_{0.2})Fe_{2-x}Ru_xO_4$ NPs where $0.00 \le x \le 0.04$. From the obtained TEM images, it is clear that the prepared samples exhibit pseudo-spherical morphology. Similar morphology was observed in a previous study, where the samples $Bi_2Fe_{4-x}Mn_xO_9$ ($0.0 \le x \le 1.0$) were synthesized using the co-precipitation route (Pooladi et al., 2019). The average particle size has been calculated using ImageJ software. The mean particle size ranges between 12.8 and 17.8 nm. The particle size decreases from 15.62 nm to 12.87 nm as x increases from 0 to 0.015, and then it increases to reach 17.85 nm as x increases from 0.02 to 0.04. The variation of the particle size analyzed from TEM results is in good agreement with the variation of crystallite size D_{SSP} obtained from XRD analysis. Nevertheless, the average particle size values obtained from TEM analysis are greater than those evaluated from XRD. This may be due to the fact that particle is formed from the agglomeration of crystallites (Seyring et al., 2009). It is known that agglomeration may occur due to the magnetic interactions among several energetic crystallites found in the ferrite NPs samples (Ansari et al., 2023).

From the HRTEM images, shown in Fig. 2 (m-r), the interplaner distance was calculated using ImageJ software. The interplanar distance corresponding to the (3 1 1) plane of the most intense peak appears in HRTEM images of all the prepared samples. Thus, the HRTEM result is in good agreement with the XRD analysis. Furthermore, the selected area electron diffraction patterns (SAED) of $(Cd_{0.4}Ni_{0.4}Mn_{0.2})Fe_{2-x}Ru_xO_4$ NPs for the six samples are also shown in Fig. 2 (s-x). These SAED patterns consist of rings having bright spots over them that ensure the polycrystalline nature of the samples (Debnath & Das, 2020). The lattice fringes enabled the calculation of the d-spacing using ImageJ software. The calculation of d-spacing gave information about the plane types. In other words, the Miller indices were determined using the values of d-spacing, and thus the average lattice parameter was calculated for each sample. As shown in Fig. 3, the values lattice parameter calculated from SAED patterns is well matched with the results of XRD patterns. As Ru^{3+} content increased from 0 to 0.04, the lattice parameter obtained from MAUD software increased from 8.462 to 8.482 Å, and the values obtained from SAED images increased from 8.69 to 8.77 Å.

3.3. SEM and EDX analysis

Scanning electron microscopy (SEM) was used to study the morphology and size of pure and Ru-doped ferrite NPs. The SEM images, shown in Fig. 4, reveal the pseudo-spherical morphology of the prepared NPs. The agglomeration might be attributed to the magnet-dipole interactions among the NPs (Köseoğlu, 2015). As a result of the enhanced aggregate of the prepared NPs, the synthesized samples may exhibit excellent electrical properties (Vinod et al., 2022). The grain sizes of $(Cd_{0.4}Ni_{0.4}Mn_{0.2})Fe_{2-x}Ru_xO_4$ NPs, estimated from SEM analysis, are 32.7, 29.6, and 30.7 nm for x = 0.00, 0.02, and 0.04, respectively. The variations of the obtained grain size from SEM analysis are similar to those estimated from XRD and TEM results. However, the values of

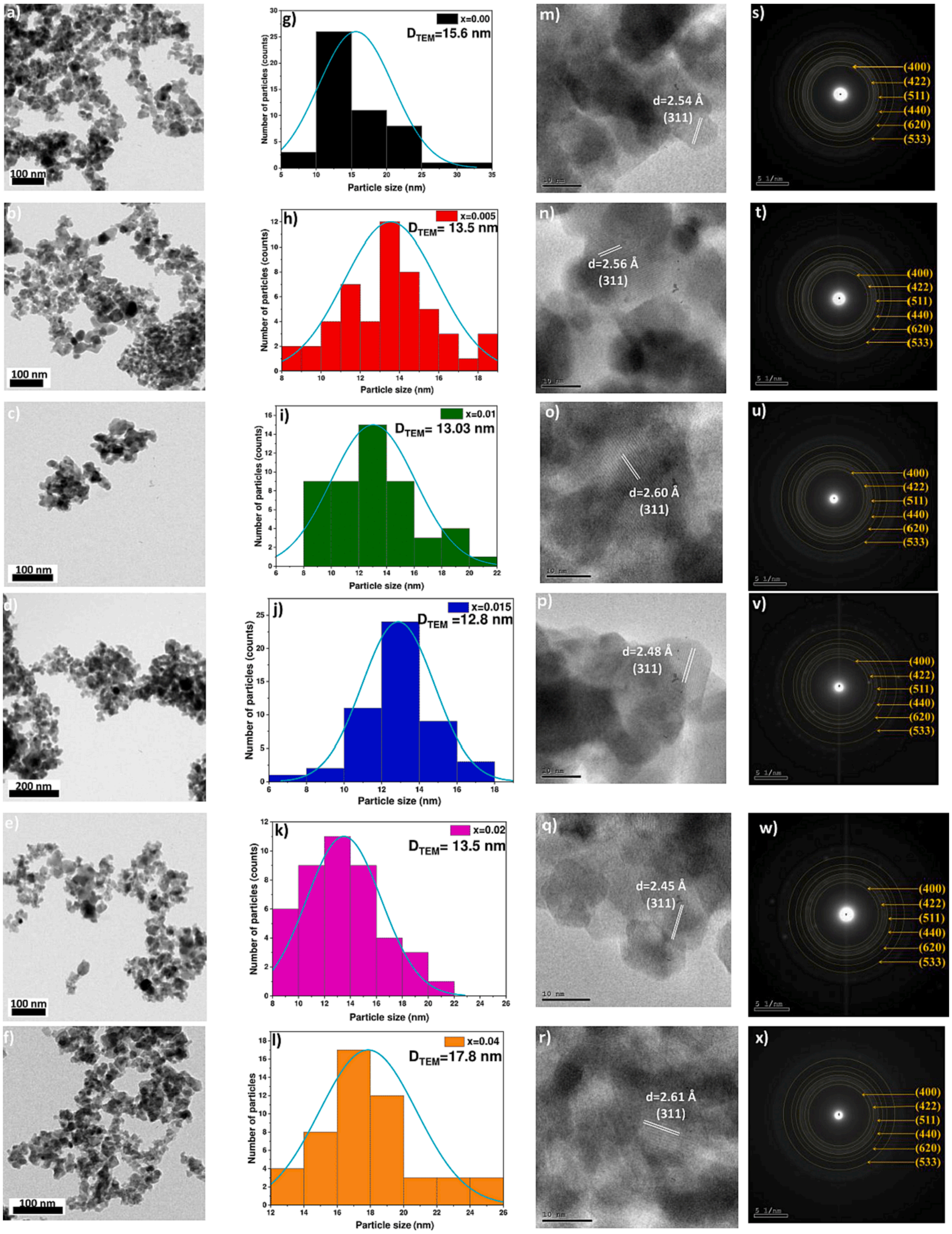

Fig. 2. (a-f) TEM, (g-l) particle size distribution, (m-r) HRTEM, and (s-x) SAED images of $(Cd_{0.4}Ni_{0.4}Mn_{0.2})Fe_{2-x}Ru_xO_4$ nanoparticles where x = 0.00, 0.005, 0.01, 0.015, 0.02 and 0.04.

particle size are greater than the values obtained from XRD and TEM analysis. Thus, this validates the TEM discussion.

The energy dispersive X-ray spectroscopy (EDX) was carried out to study and validate the elemental compositions of $(Cd_{0.4}Ni_{0.4}Mn_{0.2})Fe_{2-x}Ru_xO_4$ NPs where x = 0.00, 0.02, and 0.04. The EDX spectra, represented in Fig. 4, revealed peaks related to the presence of Cd, Ni, Mn, Fe, O, and Ru. Thus, the purity of the prepared NPs (x = 0.00, 0.02, and 0.04) was confirmed by the absence of extra peaks in the EDX spectra. The quantitative EDX analysis was performed by which the atomic percentage of elements was calculated at different regions in the sample and compared with the theoretical values as listed in Table 3. The results indicate that the elements are homogeneously distributed. The experimental atomic percentage of the elements was comparable with the theoretically calculated values. Furthermore, the substitution of the host Fe^{3+} ions by the guest Ru^{3+} ions is identified from the decrease in the atomic percentage of Fe from 27.42 to 24.33 % accompanied by the increase in the atomic percentage of Ru from 0 to 0.47 % as the Ru content increases from 0 to 0.04 as shown in Fig. 5. It is important to note that the EDX analysis was done on 3 different regions for each sample. The regions analyzed for pure $(Cd_{0.4}Ni_{0.4}Mn_{0.2})Fe_2O_4$ NPs are displayed in Fig. 6. Furthermore, the obtained atomic % for each element in $(Cd_{0.4}Ni_{0.4}Mn_{0.2})Fe_2O_4$ NPs are listed in Table 4. It is clear that a similar atomic % is revealed for each element in the analyzed regions. Consequently, the composition and distribution of elements

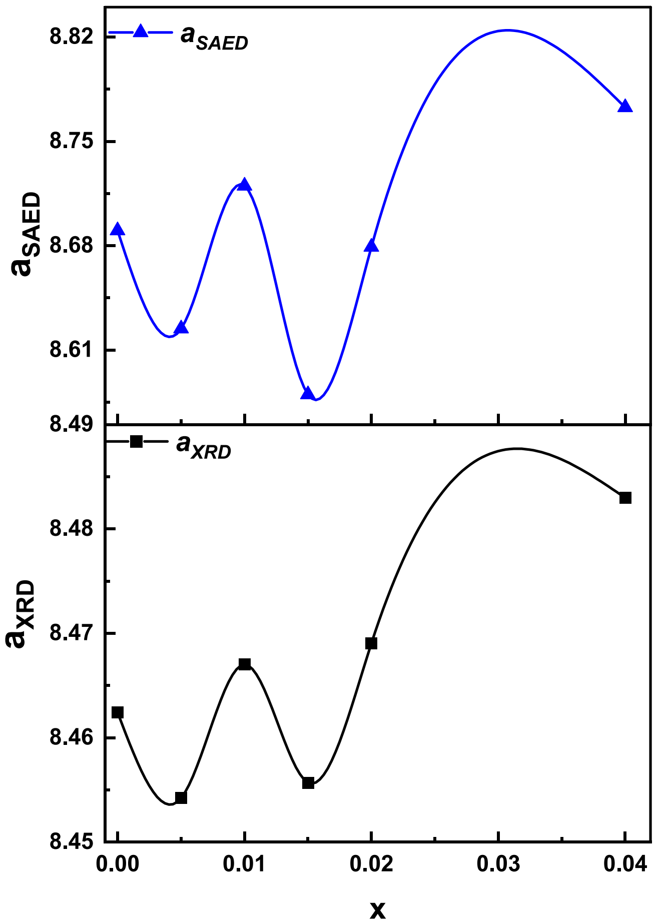

Fig. 3. Variation of lattice parameter (a_{XRD} and a_{SAED}) for $(Cd_{0.4}Ni_{0.4}Mn_{0.2})Fe_{2-x}Ru_xO_4$ NPs where x = 0.00, 0.005, 0.01, 0.015, 0.02, and 0.04.

within the nanoparticles are uniform and not significantly varied in different areas of the sample.

3.4. *Surface area measurement*

The N_2 adsorption–desorption isotherms of $(Cd_{0.4}Ni_{0.4}Mn_{0.2})Fe_{2-x}Ru_xO_4$ NPs where x = 0.00, 0.015 and 0.04 along with pore size distribution curves are shown in Fig. 7. According to the IUPAC classification, the N_2 adsorption–desorption isotherms display a type IV isotherm. Brunauer–Emmett–Teller (BET) analysis is applied to examine the surface area (S_{BET}). Whereas the pore volume and diameter are determined via the Barrett–Joyner–Halenda (BJH) model. The values of S_{BET}, pore volume, and pore diameter are listed in Table 5. As the Ru content increases from 0.00 to 0.04, S_{BET} increases from 52.39 to 78.34 m^2/g, respectively. Among the analyzed samples, $(Cd_{0.4}Ni_{0.4}Mn_{0.2})Fe_{2-x}Ru_xO_4$ NPs where x = 0.015 exhibit the highest pore volume and diameter. The pore diameter, ranging between 12.71 and 18.38 nm, reveals the mesoporous nature of the prepared samples (Aridi et al., 2023).

3.5. *UV–vis analysis*

The UV–vis absorbance spectra, represented in Fig. 8, were recorded at room temperature from 250 to 700 nm to estimate the optical bandgap energy of $(Cd_{0.4}Ni_{0.4}Mn_{0.2})Fe_{2-x}Ru_xO_4$ NPs. A major absorption peak appears in the range between 335 and 338 nm. The results of the maximum peak position are comparable with previous results at which the absorbance peak was around 300 nm (Sattar et al., 2022).

Knowing that, the highest absorbance peak of nanosized magnetic materials takes a position in the range of 200–350 nm (Sattar et al., 2022). The bandgap energy of the prepared NPs was estimated by several methods and the results are listed in Table 6. Tauc's equation was used to determine the bandgap energy and is represented as follows (Vinod et al., 2022):

$$(\alpha h\nu)^n = B(h\nu - E_g), \tag{6}$$

where $h\nu$ is the photon energy, B is the transition probability dependence constant, E_g is the optical bandgap energy and n is the nature of transition (where n = 2 and 1/2 denote the direct and indirect transitions). The following relation was used to calculate the absorption coefficient (α) (Vinod et al., 2022):

$$\alpha = \frac{2.303\,A}{d} \tag{7}$$

where A is the absorbance and d is the light path length (1 cm). Direct and indirect transitions were calculated by plotting $(\alpha h\nu)^n$ vs. E as shown in Fig. 9. As listed in Table 5, the direct and indirect bandgap energy is in the range of 3.049–3.232 eV and 1.894–2.642 eV, respectively. The obtained results are comparable to those reported in previous studies (Abdel Maksoud et al., 2021; Bhalla et al., 2021). Besides, the direct bandgap energy can be calculated by another method using the following formula:

$$E = \frac{hc}{\lambda} \tag{8}$$

where h is Planck's constant, c denotes the speed of light and λ is the wavelength obtained from Fig. 10 (a). The Urbach energy (E_U) determines the band tail width of localized states within the bandgap of NPs and can be calculated using this formula (Lemziouka et al., 2020):

$$\ln(\alpha) = \ln(\alpha_0) + \frac{h\nu}{E_U} \tag{9}$$

Knowing that α_0 is a constant. The Urbach energy, calculated from the reciprocal of the slope of the linear plot of ln (α) vs. ($h\nu$), is demonstrated in Fig. 10 (b). The obtained E_U values range between 0.44 and 0.99 eV. Comparable results were reported in previous studies, by which, the E_U values range between 0.42 and 0.6 eV (Lemziouka et al., 2020). The decrease in the E_U from 0.99 to 0.73 eV as the Ru^{3+} content increased from 0.00 to 0.04 was due to the decrease in the defects found in the doped samples (Bagi Aljewaw et al., 2020; Fernández et al., 2023).

The values of direct bandgap energy E_g and indirect bandgap energy E_{gi} increase as the Ru content increases from 0.00 to 0.015. Whereas, with further increase in Ru content (x = 0.04), the values of E_g and E_{gi} reduced. This variation of E_g and E_{gi} depends on the particle size, crystallinity, lattice constant, lattice strain, purity, nature and compositions of the dopant (Patade et al., 2020). It is worth mentioning that all doped NPs revealed lower E_U values compared to pure NPs. Thus, the defects are diminished upon doping NPs with Ru. This is in good agreement with XRD results that showed a reduction in the secondary phase percentage upon doping NPs. An inverse relation between E_g and E_U is observed as displayed in Fig. 11. Moreover, the E_g values are inversely proportional to the crystallite and particle size obtained from XRD and TEM analysis, respectively. This relationship is attributed to the variation of the lattice constant and quantum confinement effect (Singh et al., 2010). The reason behind the increase in the bandgap energy from 3.049 to 3.232 eV with the reduction in the particle size from 15.6 to 12.8 nm as x increases from 0 to 0.015 is owed to the quantum size effect (Zhou et al., 2019). Knowing that the quantum size effect leads to a blue shift of bandgap energy (Singh et al., 2010). Conversely, as x increases from 0.015 to 0.04, the particle size increases from 12.8 for to 17.8 nm whereas the energy gap decreases from 3.232 to 3.128 eV. This decrease is attributed to surface and interface effects, resulting in a red shift of the bandgap energy (Singh et al., 2010). Furthermore, similar results for the

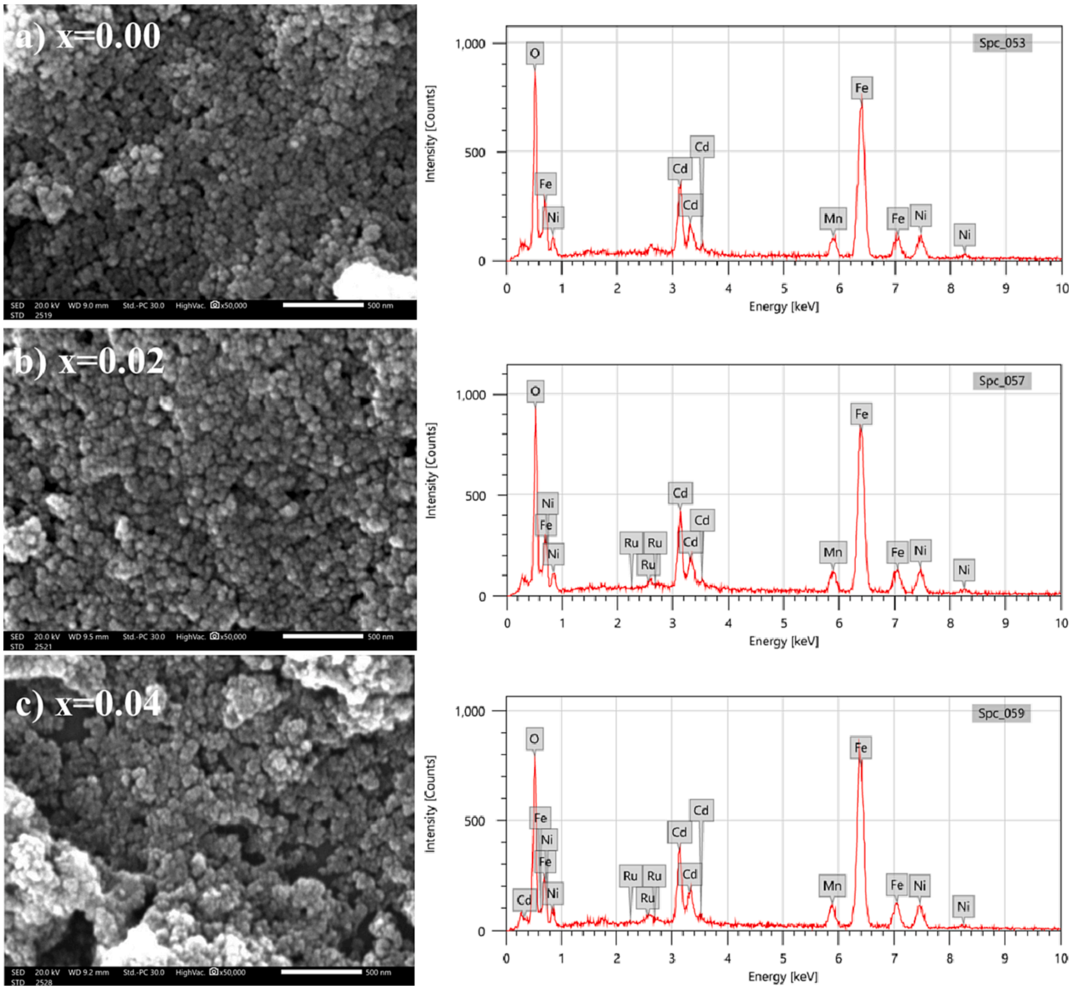

Fig. 4. SEM images and EDX spectra of $(Cd_{0.4}Ni_{0.4}Mn_{0.2})Fe_{2\text{-}x}Ru_xO_4$ NPs where (a) $x = 0.00$, (b) $x = 0.02$ and (c) $x = 0.04$.

Table 3
Experimental and theoretical values of the atomic percentages of the elements of $(Cd_{0.4}Ni_{0.4}Mn_{0.2})Fe_{2\text{-}x}Ru_xO_4$ NPs.

x	0.00	0.02	0.04
Experimental atomic percentage %			
Cd	5.18 ± 0.07	5.55 ± 0.11	5.07 ± 0.10
Ni	5.02 ± 0.17	5.42 ± 0.19	4.94 ± 0.17
Mn	2.85 ± 0.09	2.67± 0.12	2.54 ± 0.11
Fe	26.61 ± 0.33	26.35 ± 0.23	24.33 ± 0.30
Ru	0	0.20 ± 0.04	0.47 ± 0.03
O	60.36 ± 0.04	60.36 ± 0.78	63.09 ± 0.73
Theoretical atomic percentage %			
Cd	5.7	5.7	5.7
Ni	5.7	5.7	5.7
Mn	2.8	2.8	2.8
Fe	28.5	28.2	28
Ru	0	0.28	0.57
O	57.14	57.14	57.14

variation of particle size with the energy gap were observed in previous studies about $Mn_{1\text{-}x}Zn_xFe_2O_4$ where the bandgap energy increased with the increase in zinc concentration and the crystallite size decreased (Patade et al., 2020).

3.6. Adsorption performance of $(Cd_{0.4}Ni_{0.4}Mn_{0.2})Fe_{2\text{-}x}Ru_xO_4$ NPs

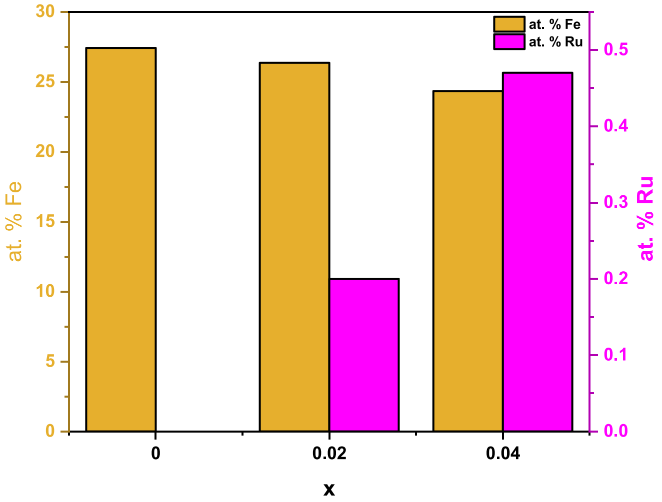

Fig. 5. Variation of the atomic % of host (Fe) and guest (Ru) with Ru content.

Doping ferrite NPs with rare earth metals improves their properties and enhances their effectiveness in wastewater treatment, particularly in dye removal (Ahmed et al., 2014; Keerthana et al., 2021). Therefore, the capability of $(Cd_{0.4}Ni_{0.4}Mn_{0.2})Fe_{2\text{-}x}Ru_xO_4$ NPs in the adsorption of CR dye was studied. For this study, 60 mg of each of $(Cd_{0.4}Ni_{0.4}Mn_{0.2})Fe_{2\text{-}x}Ru_xO_4$ NPs, where $0.00 \leq x \leq 0.04$, was mixed with 150 mL of 30 ppm CR solution. The pseudo-first-order and pseudo-second-order models were used to study the adsorption kinetics of CR and the

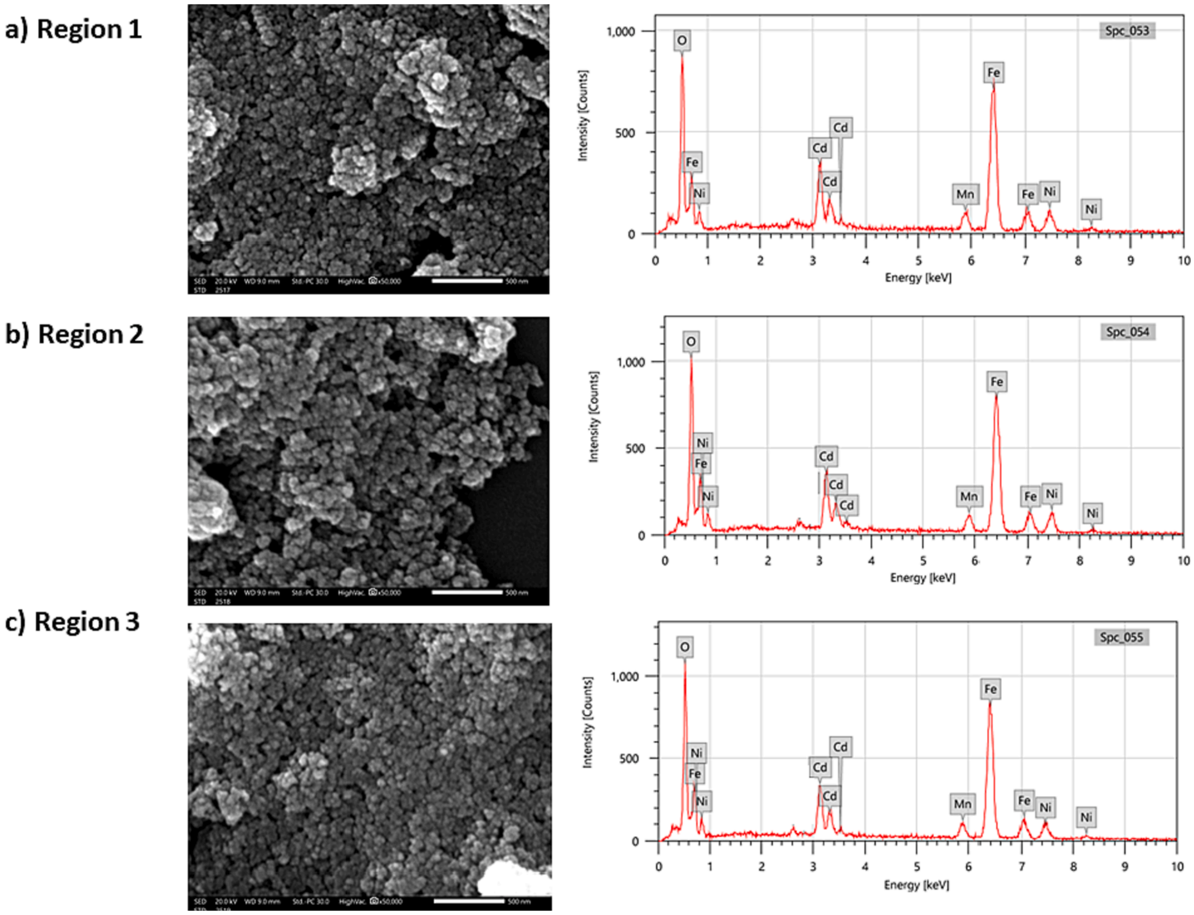

Fig. 6. SEM images and EDX spectra of $(Cd_{0.4}Ni_{0.4}Mn_{0.2})Fe_2O_4$ NPs in 3 different regions.

Table 4
Atomic percentages of the elements of $(Cd_{0.4}Ni_{0.4}Mn_{0.2})Fe_2O_4$ NPs in 3 different regions.

	Experimental atomic percentage %				
	Cd	Ni	Mn	Fe	O
Region 1	5.36	5.03	3.02	26.21	60.38
Region 2	5.12	5.37	2.90	26.19	60.42
Region 3	5.06	4.66	2.65	27.42	60.27

obtained equation and R^2 values are listed in Table 7. The first-order kinetic model is given as follows (Konicki et al., 2013):

$$\ln(q_e - q_t) = -k_1 t + \ln(q_e) \tag{10}$$

where k_1 represents the rate constant (min^{-1}) and q_e ($mg.g^{-1}$) and q_t ($mg.g^{-1}$) represent the amount of CR dye adsorbed at equilibrium and at any time t, respectively. Moreover, the second-order model is given as follows (Konicki et al., 2013):

$$\frac{t}{q_t} = \frac{1}{k_2 q_e^2} + \frac{t}{q_e} \tag{11}$$

where k_2 represents the second-order rate constant ($g.mg^{-1}.min^{-1}$). Therefore, q_e and k_2 were determined from the slope and intercept of the plot of t/q_t versus t, respectively. Higher R^2 values ($R^2 \geq 0.972$) were obtained from second-order kinetics compared to the first-order model. This suggests that the adsorption of CR dye is well described by the second-order kinetics model. Similar results were reported in previous studies where the pseudo-second-order kinetic model was used to describe the adsorption process of CR dye on the $CaFe_2O_4$ and MFe_2O_4 ($M = Co^{2+}$, Mg^{2+}, Mn^{2+}, Ni^{2+}, Zn^{2+}) (Liu et al., 2015; Roman et al., 2019). Therefore, the variation of the rate constant (k_2) of the adsorption reaction with the Ru content is represented in Fig. 12. Among the prepared NPs, the highest adsorption rate was achieved in the presence of $(Cd_{0.4}Ni_{0.4}Mn_{0.2})Fe_{2-x}Ru_xO_4$ NPs with $x = 0.015$. It is worth mentioning that $(Cd_{0.4}Ni_{0.4}Mn_{0.2})Fe_{2-x}Ru_xO_4$ NPs with $x = 0.015$ have the smallest particle size as revealed from XRD and TEM analysis. The surface area, pore size, and volume play a significant role in adsorption. Furthermore, $(Cd_{0.4}Ni_{0.4}Mn_{0.2})Fe_{2-x}Ru_xO_4$ NPs with $x = 0.015$ revealed high pore diameter and volume. Thus, larger pores provide more space for adsorbate molecules to be captured and retained, contributing to better performance. $(Cd_{0.4}Ni_{0.4}Mn_{0.2})Fe_{2-x}Ru_xO_4$ NPs with $x = 0.015$ have been used to examine the influence of contact time, adsorbent amount, pH and temperature on the adsorption rate of CR dye.

The first-order and second-order kinetics models do not provide an adequate explanation of the diffusion mechanism. Therefore, the intra-particle diffusion (IPD) model was employed in order to gain insights into the adsorption mechanism of CR dye onto $(Cd_{0.4}Ni_{0.4}Mn_{0.2})Fe_{2-x}Ru_xO_4$ NPs. The equation of the IPD model is expressed as follows (Zafar et al., 2022):

$$q_t = k_i t^{1/2} + C \tag{12}$$

where k_i ($mg.\ g^{-1}.min^{1/2}$) is the IPD rate constant and C ($mg.\ g^{-1}$) is the intercept. The values of k_i and C are listed in Table 8. The IPD model plot, displayed in Fig. 13, reveals the coexistence of two linear regions in the presence of all samples. Thus, multiple stages are involved in the adsorption process of CR. Furthermore, the k_i values of the first region are greater than that of the second region. The first region in the IPD plot reveals the rapid diffusion stage accompanied by external surface

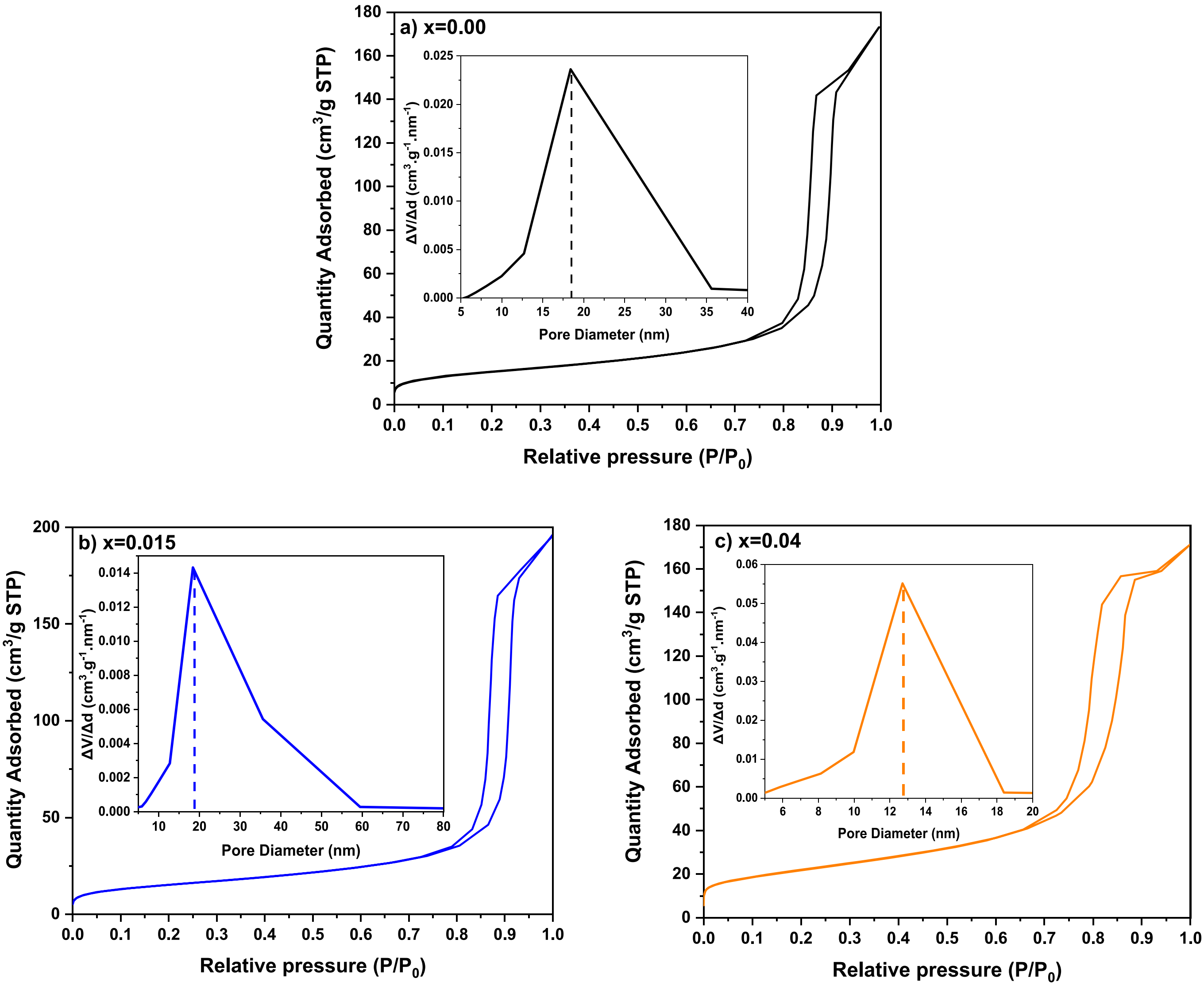

Fig. 7. N_2 adsorption–desorption isotherms along with pore size distribution curves of $(Cd_{0.4}Ni_{0.4}Mn_{0.2})Fe_{2\text{-}x}Ru_xO_4$ NPs where (a) x = 0.00, (b) x = 0.015, and (c) x = 0.04.

Table 5
Surface area (S_{BET}), pore volume, and pore diameter of $(Cd_{0.4}Ni_{0.4}Mn_{0.2})Fe_{2\text{-}x}Ru_xO_4$ NPs with x = 0.00, 0.015, and 0.04.

x	S_{BET} (m^2/g)	Pore volume (cm^3/g)	Pore diameter (nm)
0.00	**52.39**	**0.32**	**16.81**
0.015	54.15	0.39	18.38
0.04	78.34	0.26	12.71

adsorption of CR. However, the second region in the plot shows a slow adsorption stage which is associated with the intraparticle diffusion of CR within the pores of the $(Cd_{0.4}Ni_{0.4}Mn_{0.2})Fe_{2\text{-}x}Ru_xO_4$ adsorbents (Zafar et al., 2022). Since C exhibits non-zero values, intra-particle diffusion is not the only rate-limiting step (Lafi et al., 2019). The contribution of surface adsorption is revealed from the large values of C.

3.6.1. *Effect of contact time*

By determining the optimal contact time, the efficiency of dye removal will be improved and the wastewater treatment time will be minimized. The influence of the contact time on the removal % of CR was studied by mixing 60 mg of $(Cd_{0.4}Ni_{0.4}Mn_{0.2})Fe_{1.985}Ru_{0.015}O_4$ adsorbent with 150 mL of 30 ppm CR dye solution. The removal %, displayed in Fig. 14, was determined using the following formula:

$$\text{Removal}\,\% = \frac{C_0 - C_t}{C_0} \times 100, \tag{13}$$

As the contact time increases to 180 min, the removal percentage also increases until it reaches 59.03 %. With a further increase in the contact time, the removal % increases to reach 60.73 % after 240 min. A comparison with previous studies, as listed in Table 9, clearly indicates that the synthesized nanoparticles $(Cd_{0.4}Ni_{0.4}Mn_{0.2})Fe_{1.985}Ru_{0.015}O_4$ have the highest removal % and adsorption capacity. This reveals that $(Cd_{0.4}Ni_{0.4}Mn_{0.2})Fe_{1.985}Ru_{0.015}O_4$ is an effective adsorbent for the removal of CR dye. Consequently, tri-metal ferrite nanoparticles exhibit superior adsorption performance compared to single and di-metal ferrite nanoparticles.

3.6.2. *Effect of adsorbent amount*

To examine the influence of adsorbent amount on the rate of CR adsorption, various amounts (20, 40, 60, 80, and 100 mg) of $(Cd_{0.4}Ni_{0.4}Mn_{0.2})Fe_{1.985}Ru_{0.015}O_4$ adsorbent were mixed with 150 mL of 30 ppm CR dye solution. Following the second-order kinetic model, the adsorption rate (k_2) was calculated. The results, displayed in Fig. 15, reveal that the rate constant is boosted from 0.75×10^{-3} to reach 5.51 ×

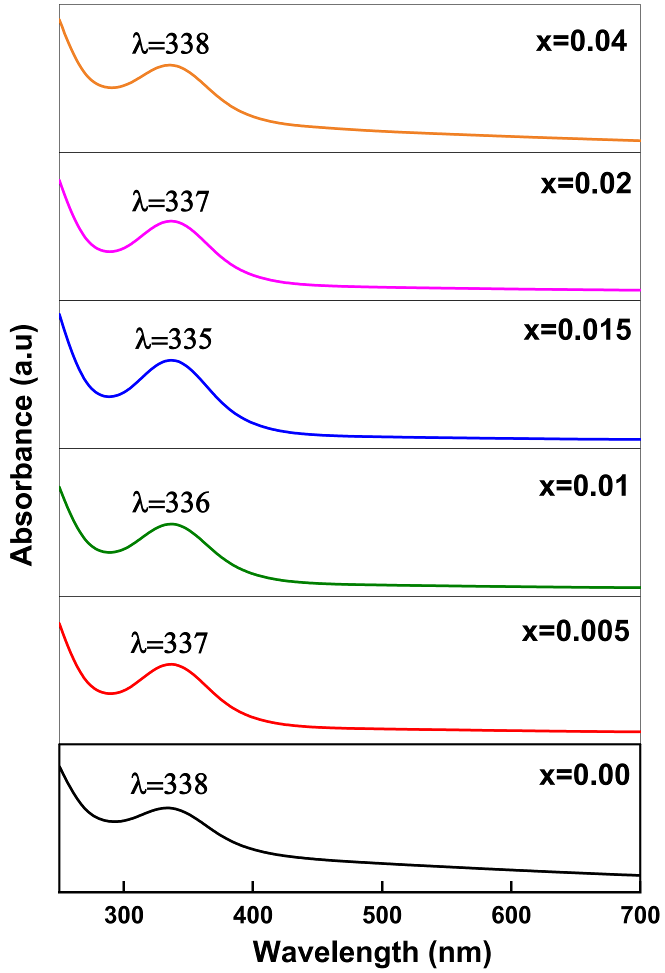

Fig. 8. UV absorption spectra of $(Cd_{0.4}Ni_{0.4}Mn_{0.2})Fe_{2\text{-}x}Ru_xO_4$NPs.

Table 6
Values of direct and indirect bandgap energy and Urbach energy (E_U) of $(Cd_{0.4}Ni_{0.4}Mn_{0.2})Fe_{2\text{-}x}Ru_xO_4$ NPs.

x	E_g Tauc's plot eV	E_g Absorbance eV	E_{gi} eV	E_U eV
0.00	3.049 ± 0.009	2.796 ± 0.004	1.894 ± 0.001	0.992 ± 0.009
0.005	3.215 ± 0.003	2.876 ± 0.002	2.572 ± 0.005	0.487 ± 0.005
0.01	3.223 ± 0.002	2.927 ± 0.003	2.606 ± 0.009	0.465 ± 0.004
0.015	3.232 ± 0.003	2.934 ± 0.002	2.642 ± 0.005	0.441 ± 0.004
0.02	3.221 ± 0.003	2.928 ± 0.002	2.598 ± 0.004	0.470 ± 0.009
0.04	3.128 ± 0.004	2.895 ± 0.003	2.214 ± 0.007	0.739 ± 0.002

10^{-3} g.mg^{-1}.min^{-1} as the adsorbent amount increases from 20 to 80 mg, respectively. This is due to the increase in the active sites upon increasing the adsorbent amount (Ali et al., 2018; Zeng et al., 2014). Whereas, the rate constant is diminished from 5.51 × 10^{-3} to reach 3.65 × 10^{-3} g.mg^{-1}.min^{-1} as the adsorbent amount increased from 80 to 100 mg. This might be attributed to the aggregation of NPs in the presence of excess amounts leading to a reduction in the adsorption efficiency (Panda et al., 2021). Therefore, 80 mg is the optimum adsorbent amount of $(Cd_{0.4}Ni_{0.4}Mn_{0.2})Fe_{1.985}Ru_{0.015}O_4$ used for the adsorption of CR dye.

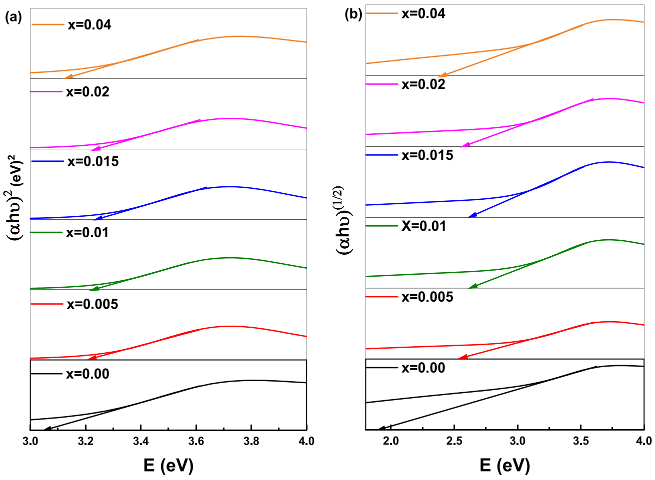

Fig. 9. Tauc's plot of $(Cd_{0.4}Ni_{0.4}Mn_{0.2})Fe_{2\text{-}x}Ru_xO_4$ NPs used to determine (a) direct bandgap energy and (b) indirect bandgap energy.

3.6.3. *Effect of pH*

Varying pH is an important factor that has a vital role in the adsorption mechanism since it regulates the charges of the adsorbent that affect the interaction with dye molecules (Wekoye et al., 2020). Consequently, the adsorption experiments have been carried out in the presence of 60 mg of $(Cd_{0.4}Ni_{0.4}Mn_{0.2})Fe_{1.985}Ru_{0.015}O_4$ adsorbent in different mediums where the pH ranges between 2.99 and 11.01. The obtained results are displayed in Fig. 16. The rate constant of the adsorption reaction increased from 2.12 × 10^{-3} to 4.81 × 10^{-3} g.mg^{-1}.min^{-1} as the pH increased from 2.99 to 3.45. Whereas, as the pH increased from 3.45 to 11.01, the rate constant decreased to reach 1.33 × 10^{-3} g.mg^{-1}.min^{-1}. As documented in previous studies, the point of zero charge (PZC) of $CdFe_2O_4$, $NiFe_2O_4$, and $MnFe_2O_4$ NPs were 6.9, 6.4, and 6.5 respectively (Douafer et al., 2023; Eyvazi et al., 2020; Fathy et al., 2022). It is known that NPs are positively charged in an acidic medium ($pH < PZC$) and negatively charged in a basic medium ($pH > PZC$) (An et al., 2015; Chauhan et al., 2020). Furthermore, CR, as an anionic dye, carries a negative charge. Thus, the electrostatic attraction between the positively charged NPs and the negatively charged CR dye molecules promotes adsorption which in turn boosts the rate of the adsorption process in an acidic medium (Sachin et al., 2023). In other words, opposite charges attract each other, leading to a higher affinity and stronger binding between the dye and the positively charged NPs. Conversely, at high pH, when both the dye and the NPs' surface carry negative charges, the repulsion between them reduces the adsorption capacity and weakens the adsorption process (Chauhan et al., 2020). Thus, the highest adsorption rate of CR is achieved in an acidic medium where pH = 3.45. The results are comparable to previous studies that studied the adsorption capacity of cobalt ferrite NPs for the removal of CR dye at different pH values, and the highest adsorption rate was achieved in an acidic medium (Simonescu et al., 2021). By this, the adsorption capacity increased as the pH value increased to 4.5, and then it decreased as the pH increased up to 11.

3.6.4. *Effect of temperature*

To understand the temperature dependence, adsorption experiments were conducted at different temperatures (303, 308, 313, 318, and 323 K) in the presence of 60 mg of $(Cd_{0.4}Ni_{0.4}Mn_{0.2})Fe_{1.985}Ru_{0.015}O_4$ adsorbent mixed with 150 mL of 30 ppm CR dye solution. The results, displayed in Fig. 17, show that as the reaction temperature increased from 303 to 308 K, the rate constant increased from 1.74 × 10^{-3} to 4.52 × 10^{-3} g.mg^{-1}.min^{-1}. It's worth noting that increasing the reaction temperature provides energy, increases the mobility of the NPs and dye molecules, and improves the adsorption process (Panda et al., 2021).

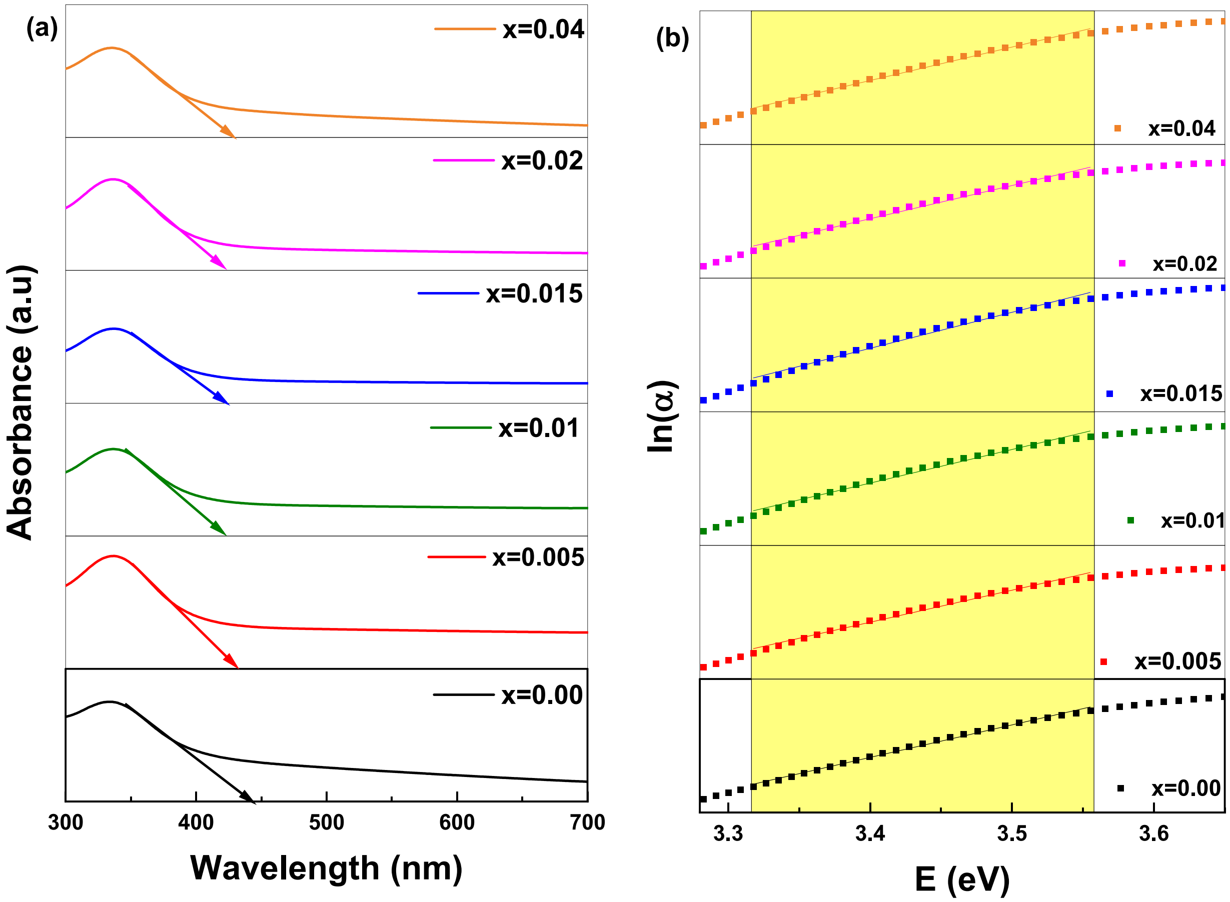

Fig. 10. Plot of (a) direct bandgap energy determined from absorbance and (b) Urbach energy (E_U) determination of $(Cd_{0.4}Ni_{0.4}Mn_{0.2})Fe_{2\text{-}x}Ru_xO_4$ NPs.

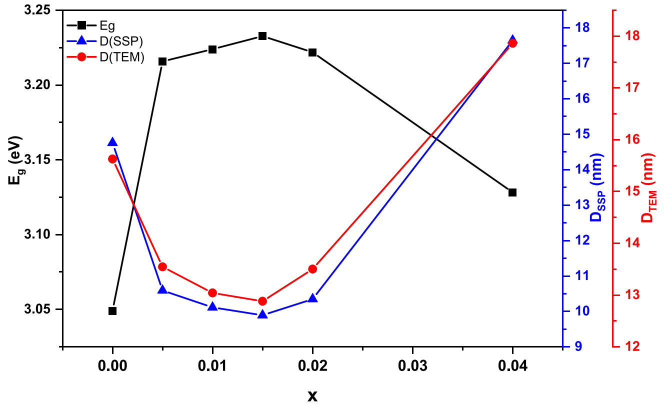

Fig. 11. Variation of bandgap energy and particle size (D_{TEM} and D_{SSP}) of $(Cd_{0.4}Ni_{0.4}Mn_{0.2})Fe_{2\text{-}x}Ru_xO_4$ NPs where $0.00 \leq x \leq 0.04$.

Table 7
Equations and R^2 values of first-order and second-order kinetics.

x	First-order kinetics		Second-order kinetics	
	Equation	R^2	Equation	R^2
0	$y = -0.0179x + 3.5024$	0.688	$y = 0.0155x + 0.2219$	0.972
0.005	$y = -0.0176x + 3.5451$	0.929	$y = 0.0136x + 0.1184$	0.997
0.01	$y = -0.0196x + 3.7622$	0.947	$y = 0.0127x + 0.1416$	0.995
0.015	$y = -0.0079x + 3.1322$	0.737	$y = 0.0181x + 0.1212$	0.986
0.02	$y = -0.0133x + 3.0767$	0.945	$y = 0.0197x + 0.1532$	0.997
0.04	$y = -0.0025x + 3.5635$	0.630	$y = 0.0133x + 0.0895$	0.997

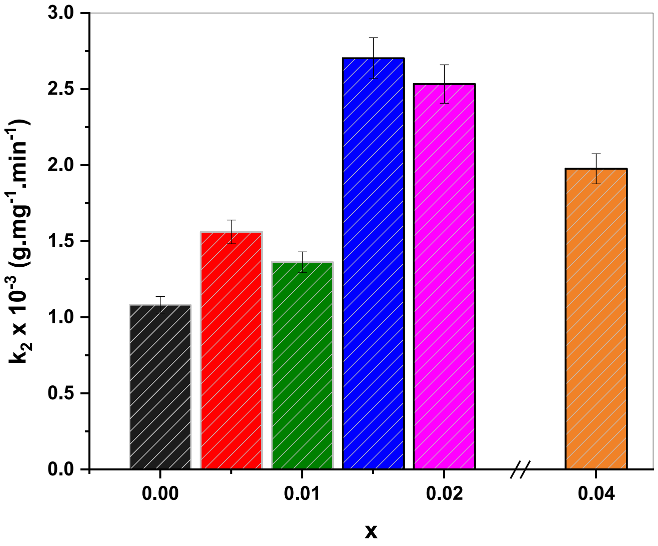

Fig. 12. The adsorption rate constant (k_2) of CR in the presence of $(Cd_{0.4}Ni_{0.4}Mn_{0.2})Fe_{2\text{-}x}Ru_xO_4$ NPs where x = 0.00, 0.005, 0.015, 0.02, and 0.04.

However, the rate constant is diminished to 1.43×10^{-3} g.mg^{-1}.min^{-1} with a further increase in the reaction temperature to reach 323 K. Thus, increasing the reaction temperature above 308 K is unfavorable for CR adsorption. This result is comparable to previous studies where 35 °C represents the best temperature for the removal of CR dye from an aqueous system (Muedi et al., 2022).

Table 8
Values k_i and C estimated from linear regions of the IPD model plot.

x		0.00	0.005	0.01	0.015	0.02	0.04
Region 1	k_i	3.03	3.35	7.15	3.02	2.73	3.81
	C	25.37	33.58	12.02	26.38	20.87	28.91
Region 2	k_i	1.76	1.44	1.12	1.11	1.16	2.04
	C	36.19	50.04	59.39	40.17	32.53	44.19

3.6.5. *Thermodynamic parameters*

Thermodynamic parameters can be determined by conducting adsorption experiments at different temperatures. These parameters include the change in the enthalpy (ΔH^0), the change in the entropy (ΔS^0) and the change in the Gibbs free energy (ΔG^0) and are listed in Table 10. The following equations are used to determine the thermodynamic parameters (Etemadinia et al., 2019; Subbaiah Munagapati et al., 2022):

$$\ln K_d = -\frac{\Delta H^0}{RT} + \frac{\Delta S^0}{R} \tag{14}$$

$$Kd = \frac{C_{ac}}{C_e} \tag{15}$$

$$\Delta G^0 = -RT\ln K_d \tag{16}$$

where K_d represents the equilibrium constant, C_{ac} (mg/L) is the adsorbed concentration of CR at equilibrium, C_e (mg/L) denotes the equilibrium concentration of CR in the solution, R represents the universal gas constant (8.314 $J.mol^{-1}.K^{-1}$) and T represents the temperature in (K). By plotting ln K_d versus 1/T, represented in Fig. 18, ΔH^0 and ΔS^0 can be calculated from the slope and intercept, respectively. The negative value of ΔH^0 indicates that the adsorption reaction is exothermic which is in agreement with the decrease in the rate constant as the temperature increases (Zeng et al., 2014). The adsorption process of CR onto $(Cd_{0.4}Ni_{0.4}Mn_{0.2})Fe_{1.985}Ru_{0.015}O_4$ nanoparticles is characterized by the heat of reaction of 14.02 $kJ.mol^{-1}$ revealing that the adsorption process involves physisorption (Subbaiah Munagapati et al., 2022). Besides, the negative value of ΔS^0 reveals the disorder decreases during the adsorption reaction. In addition, the negative values of ΔG^0 reflect the spontaneous adsorption of CR dye on the $(Cd_{0.4}Ni_{0.4}Mn_{0.2})Fe_{1.985}Ru_{0.015}O_4$ nanoparticles. These results are in good agreement with previously reported studies that show negative values of thermodynamic parameters for the removal of CR dye using $Ni_{0.6}Fe_{2.4}O_4$ nanoparticles (Zeng et al., 2014).

3.6.6. *Optimum experimental conditions for CR adsorption*

Optimized experimental conditions, mainly optimum adsorbent amount, pH, and temperature, were applied. To do so, 80 mg of

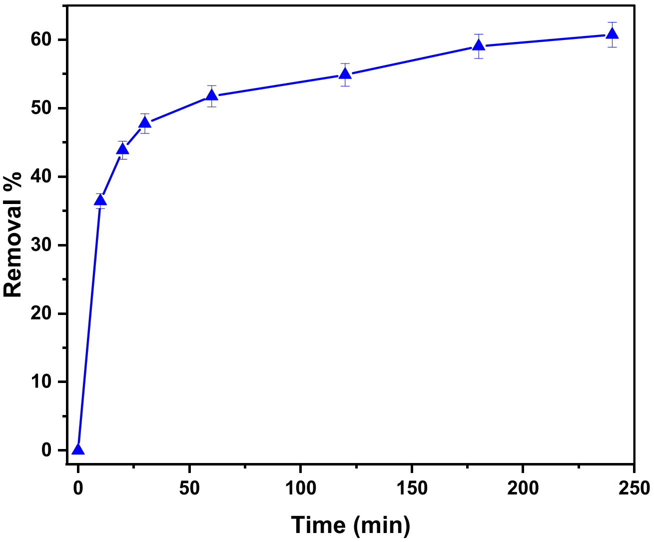

Fig. 14. Effect of contact time on the removal of CR examined in the presence of $(Cd_{0.4}Ni_{0.4}Mn_{0.2})Fe_{1.985}Ru_{0.015}O_4$ adsorbent.

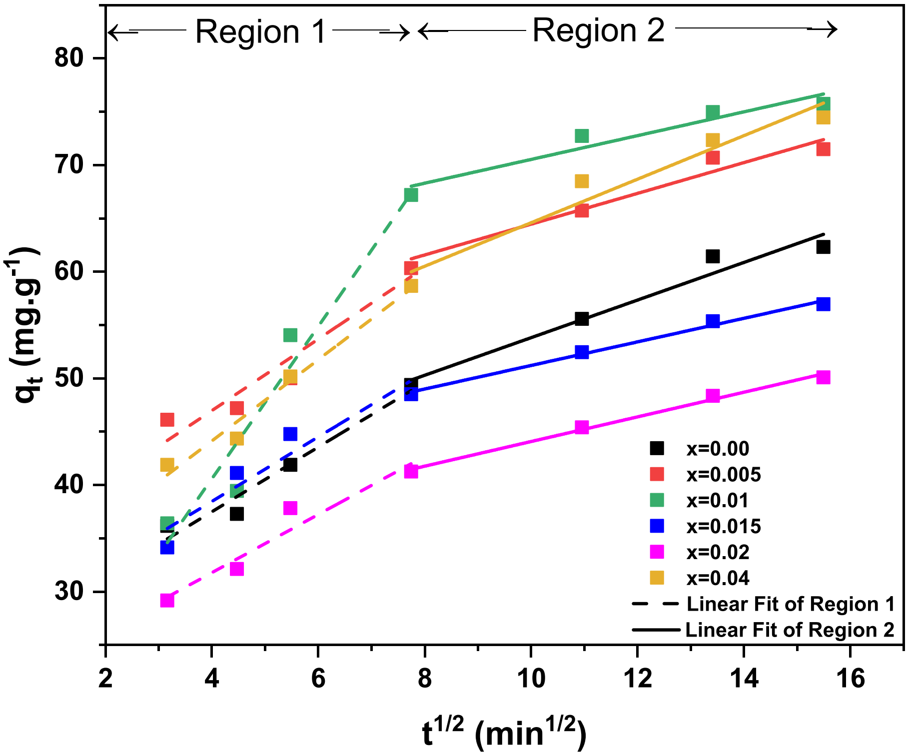

Fig. 13. IPD model applied on CR adsorption data in the presence of $(Cd_{0.4}Ni_{0.4}Mn_{0.2})Fe_{2-x}Ru_xO_4$ ($0.00 \leq x \leq 0.04$) adsorbents.

Table 9
Previous studies about the removal of CR dye in the presence of different ferrite nanoparticles.

Adsorbent	Adsorbent Dosage	CR dye concentration ppm	Removal %	Time min	qe mg/g	Ref.
$Cu_{0.5}Co_{0.5}Fe_2O_4$	50 mg	100	–	–	38.69	(Liu et al., 2022)
$MnFe_2O_4$	100 mg	30	–	–	7.497	(Yang et al., 2014)
$NiFe_2O_4$	50 mg	30	–	–	38.47	(Tan et al., 2020)
$MnFe_2O_4$	0.05 g/L	62	–	–	11.1	(Pham, T. Nguyen, et al., 2019)
$NiFe_2O_4$	1 g/L	50	23 %	180	11.4	(Samoila et al., 2015)
$ZnFe_2O_4$			12 %		5.1	
$CoFe_2O_4$			19 %		10	
$(Cd_{0.4}Ni_{0.4}Mn_{0.2})Fe_{1.985}Ru_{0.015}O_4$	60 mg	30	59.03 60.73	180 240	56.95	This study

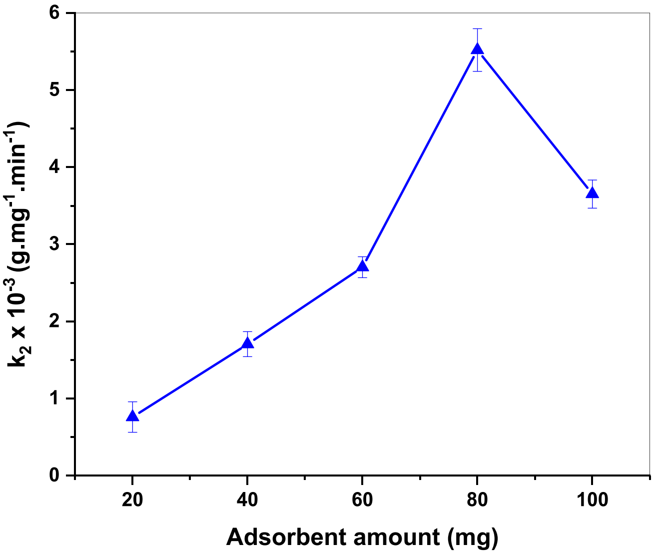

Fig. 15. Effect of $(Cd_{0.4}Ni_{0.4}Mn_{0.2})Fe_{1.985}Ru_{0.015}O_4$ adsorbent amount on adsorption rate of CR dye.

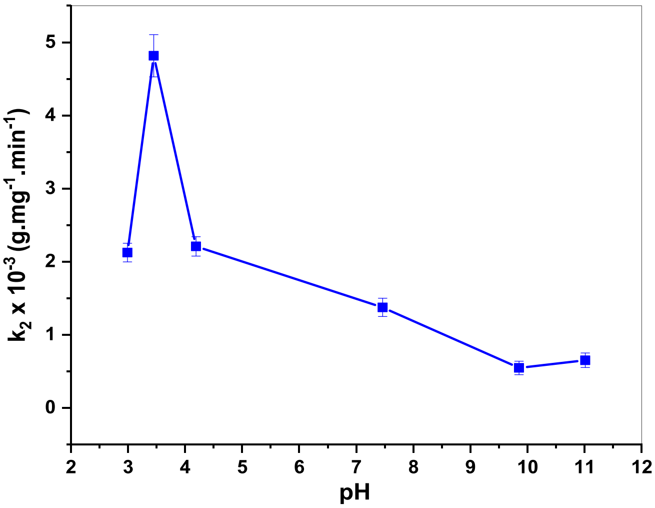

Fig. 16. Effect of pH on rate constant (k_2) of CR dye adsorption examined in the presence of $(Cd_{0.4}Ni_{0.4}Mn_{0.2})Fe_{1.985}Ru_{0.015}O_4$ adsorbent.

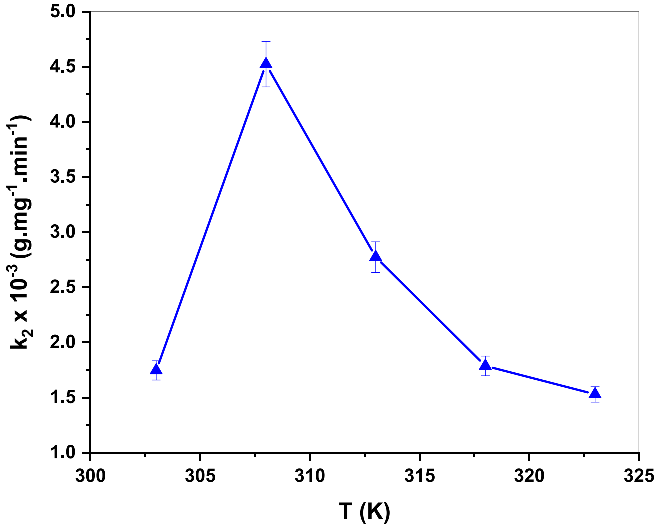

Fig. 17. Effect of temperature on rate constant (k_2) of the adsorption process of CR dye using $(Cd_{0.4}Ni_{0.4}Mn_{0.2})Fe_{1.985}Ru_{0.015}O_4$ adsorbent.

Table 10
Thermodynamic parameters for the adsorption reaction of CR dye in the presence of $(Cd_{0.4}Ni_{0.4}Mn_{0.2})Fe_{1.985}Ru_{0.015}O_4$ adsorbent.

T K	ΔH^o kJ.mol^{-1}	ΔS^o J.mol^{-1}.K^{-1}	ΔG^o J.mol^{-1}
308	−14.02	−26.94	−5683.84
313			−5648.78
318			−5430.89
323			−5305.12

$(Cd_{0.4}Ni_{0.4}Mn_{0.2})Fe_{1.985}Ru_{0.015}O_4$ NPs were mixed with 150 mL of 30 ppm CR dye solution having a pH value of 3.45 at 308 K. The results of this experiment, carried out three times, are represented in Fig. 19. The adsorption rate constant was estimated to be 10.7×10^{-3} g.mg^{-1}.min^{-1}. Furthermore, 87.5 and 88.5 % of CR dye was adsorbed after 60 and 120 min, respectively, as displayed in Fig. 19 (b). Thus, the rate of adsorption reaction and removal % are boosted upon applying the optimum experimental conditions.

3.6.7. *Reusability of $(Cd_{0.4}Ni_{0.4}Mn_{0.2})Fe_{1.985}Ru_{0.015}O_4$ adsorbent*

The regeneration ability and stability of adsorbents are key factors in determining the practicality and effectiveness of adsorption processes (Hassan et al., 2020; M. El-Metwaly et al., 2022). It promotes sustainability, cost-effectiveness, and resource conservation while enabling more efficient and reliable industrial processes and environmental remediation efforts (Almahri et al., 2023a). Therefore, the reusability of $(Cd_{0.4}Ni_{0.4}Mn_{0.2})Fe_{1.985}Ru_{0.015}O_4$ adsorbent was studied by applying the optimum experimental conditions for 4 consecutive cycles. As displayed in Fig. 20, around 87.5 % of CR dye was adsorbed in the 4 cycles. The adsorbent regeneration was achieved by rinsing first with ethanol solution and then with water (Pham et al., 2019). Knowing that $(Cd_{0.4}Ni_{0.4}Mn_{0.2})Fe_{1.985}Ru_{0.015}O_4$ adsorbents are magnetic

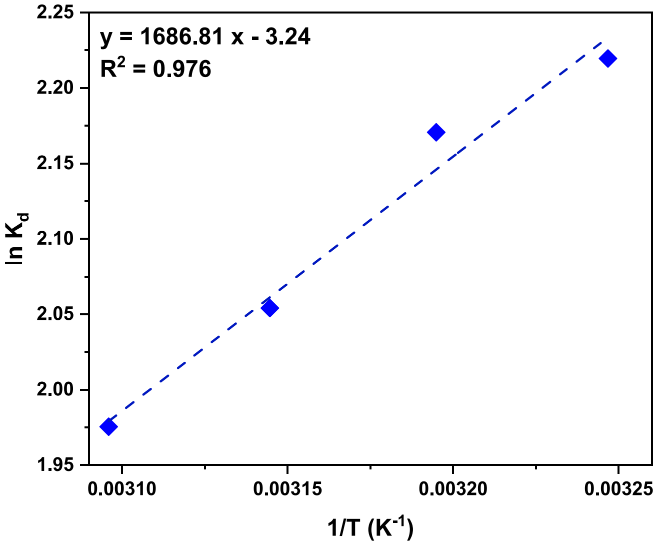

Fig. 18. Plot of $\ln K_d$ versus 1/T.

nanoparticles, they were easily separated from the solution by using a magnet without the need for centrifugation or filtration. $(Cd_{0.4}Ni_{0.4}Mn_{0.2})Fe_{1.985}Ru_{0.015}O_4$ adsorbent can be used for up to 4 cycles without a significant loss in the adsorption activity as demonstrated in Fig. 20. Thus, the prepared adsorbent preserves an improved adsorption activity after reusing.

3.6.8. Adsorption isotherms

Adsorption isotherms are essential to determine the adsorption phenomena between the CR dye and $(Cd_{0.4}Ni_{0.4}Mn_{0.2})Fe_{1.985}Ru_{0.015}O_4$ adsorbent, and to gain more insight about the mechanism of adsorption. Therefore, the adsorption reaction was carried out in the presence of 60 mg of $(Cd_{0.4}Ni_{0.4}Mn_{0.2})Fe_{1.985}Ru_{0.015}O_4$ adsorbent with varying the initial concentration of CR dye (0–50 ppm). For the present adsorbate-adsorbent system, three non-linear adsorption isotherms models were used mainly Langmuir, Freundlich, and Temkin and the results are displayed in Fig. 21. The Langmuir adsorption isotherm model proposed that there is no intermolecular interaction between the adsorbate molecules and the adsorption of CR dye molecule is only limited to monolayer (Li et al., 2021; Mishra et al., 2020). In other words, adsorption occurs only when the dye molecules collide with the surface of $(Cd_{0.4}Ni_{0.4}Mn_{0.2})Fe_{1.985}Ru_{0.015}O_4$ adsorbent (Li et al., 2021). The equation of Langmuir isotherm (Simonescu et al., 2021):

$$q_e = \frac{Q_L\, b_L C_e}{1 + b_L C_e}, \tag{17}$$

where Q_L (mg.g^{-1}) is the maximum monolayer adsorption capacity of $(Cd_{0.4}Ni_{0.4}Mn_{0.2})Fe_{1.985}Ru_{0.015}O_4$ adsorbent and b_L (L.mg^{-1}) is the Langmuir constant. Regarding the Freundlich adsorption isotherm model, it is valid for heterogeneous surface of adsorption and describes multilayer adsorption with the interaction between the adsorbed molecules (Aridi et al., 2023). The equation is expressed as follows (Simonescu et al., 2021):

$$q_e = K_F C_e{}^{1/n} \tag{18}$$

where n represents the adsorption intensity and K_F ((mg.g^{-1})(mg.L^{-1})$^{1/n}$) denotes the Freundlich constant. The Temkin model takes into account adsorbate-adsorbent molecules interaction (Mishra et al., 2020). The equation of this model is expressed as follows (Liu et al., 2022):

$$q_e = \frac{RT}{b_T}\ln(K_T C_e) \tag{19}$$

where b_T (J.mol^{-1}) represents the coefficient related to the sorption heat, and K_T (L.mg^{-1}) represents the equilibrium binding constant. The values of the adsorption isotherm parameters determined via nonlinear fitting of Langmuir, Freundlich, and Temkin models along with the coefficient of determination (R^2) are listed in Table 11. The low R^2 value obtained for the Langmuir model ($R^2 = 0.682$) along with the negative value of the Langmuir constant (b_L = -1.55) reveals the failure of this model in explaining the adsorption. However, greater R^2 values were obtained from the fitting of the Temkin model ($R^2 = 0.979$ compared to that of the Freundlich model ($R^2 = 0.957$). Thus, the Temkin model was the best-fitted model to explain the mechanism of the multilayer adsorption of CR onto $(Cd_{0.4}Ni_{0.4}Mn_{0.2})Fe_{1.985}Ru_{0.015}O_4$ nanoparticles. Additionally, the adsorption intensity value (n = 3.72) is below 10 which signifies that the adsorption of CR is favorable. The strong interactive force between CR and $(Cd_{0.4}Ni_{0.4}Mn_{0.2})Fe_{1.985}Ru_{0.015}O_4$ nanoparticles is revealed from the high value of b_T. Similar results were obtained in a previous study where the Temkin model best fitted the adsorption data of CR onto $Cu_{0.5}Co_{0.5}Fe_2O_4$ nanoparticles (Liu et al., 2022).

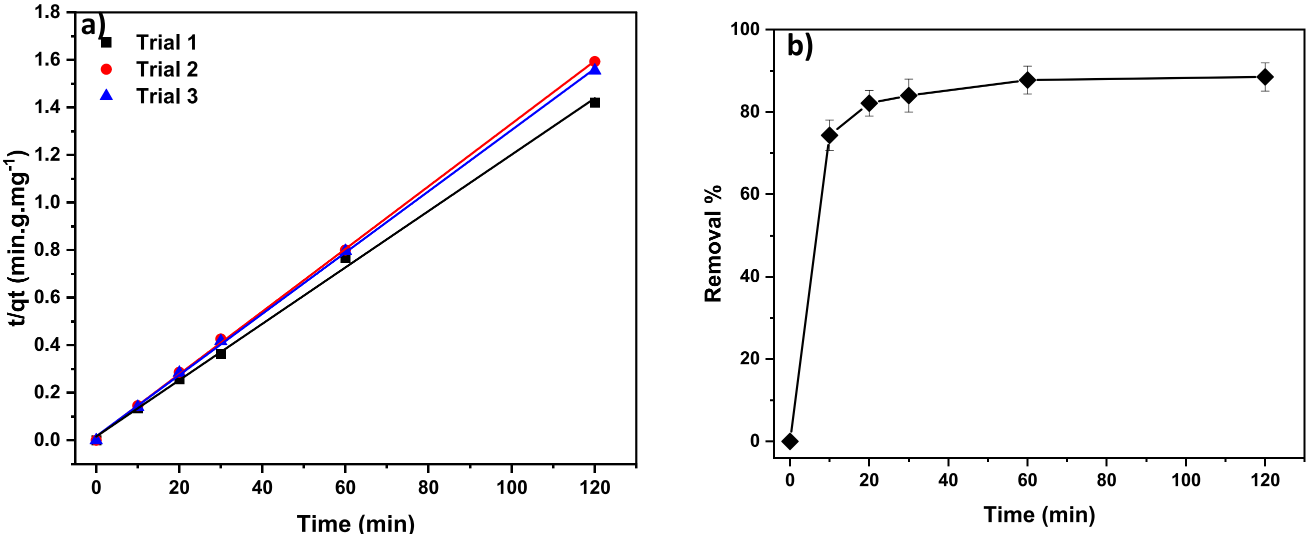

Fig. 19. (a) The kinetic plot of t/q_t and (b) removal % versus time in the presence of $(Cd_{0.4}Ni_{0.4}Mn_{0.2})Fe_{1.985}Ru_{0.015}O_4$ adsorbent.

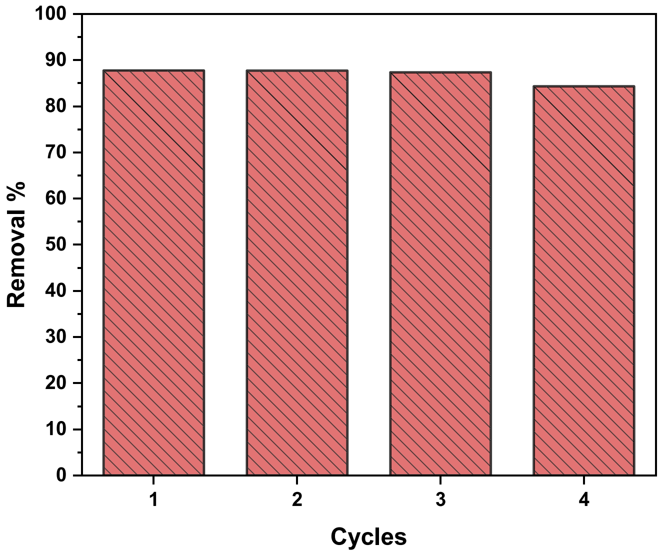

Fig. 20. Reusability of $(Cd_{0.4}Ni_{0.4}Mn_{0.2})Fe_{1.985}Ru_{0.015}O_4$ adsorbent for CR adsorption.

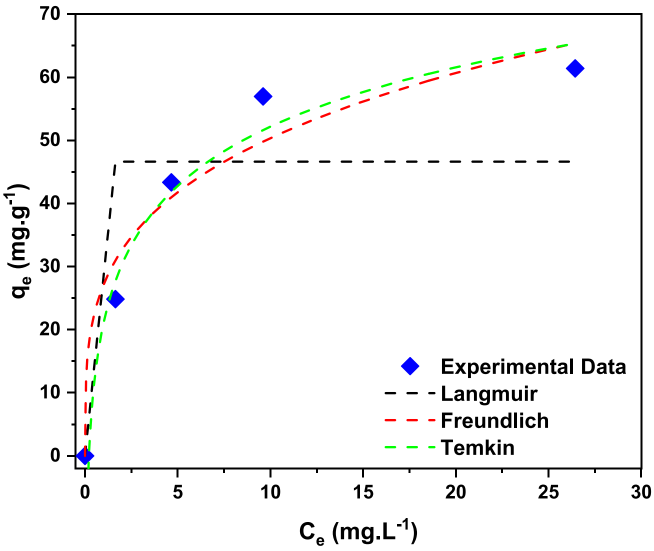

Fig. 21. The fitting plots of non-linear Langmuir, Freundlich, and Temkin isotherm for adsorption of CR on $(Cd_{0.4}Ni_{0.4}Mn_{0.2})Fe_{1.985}Ru_{0.015}O_4$ adsorbent.

Table 11
Adsorption isotherm parameters determined via nonlinear fitting of Langmuir, Freundlich, and Temkin models.

Isotherm model	Parameter	Parameter value
Langmuir	Q_L (mg.g^{-1})	46.64
	b_L (L.mg^{-1})	−1.55
	R^2	0.682
Freundlich	K_F ((mg.g^{-1})(mg.L^{-1})$^{1/n}$)	27.09
	N	3.72
	R^2	0.957
Temkin	K_T (L.mg^{-1})	4.71
	b_T (J.mol^{-1})	182.91
	R^2	0.979

4. Conclusion

$(Cd_{0.4}Ni_{0.4}Mn_{0.2})Fe_{2\text{-}x}Ru_xO_4$ NPs $(0.00 \leq x \leq 0.04)$ were successively prepared by the co-precipitation method. Upon increasing the Ru^{3+} content, the percentage of the hematite phase decreased. This confirmed the successful incorporation of the dopants' ions with the nanoferrites without forming secondary phases. The mean particle size of the prepared NPs ranged between 12 and 17 nm as revealed from the TEM analysis. Besides, the SEM analysis revealed the pseudo-spherical morphology of the NPs. The elemental composition of the ferrite nanoparticles was validated and the experimental atomic percentage of the elements was comparable with the theoretically calculated values. The direct and indirect bandgap energy and the Urbach energy of the synthesized ferrite NPs were in the range of 3.05–3.23 eV, 1.89–2.64 eV, and 0.99–0.73 eV, respectively. Among the prepared samples, the sample with x = 0.015 showed the highest adsorption rate and 60.73 % of CR dye was removed after 240 min. The adsorption rate of this sample was examined at different conditions, and it revealed that the best adsorption conditions were 80 mg of adsorbent amount, 308 K and a pH of 3.45. $(Cd_{0.4}Ni_{0.4}Mn_{0.2})Fe_{2\text{-}x}Ru_xO_4$ NPs with x = 0.015 preserved an improved adsorption activity after being reused for 4 cycles. Furthermore, different models were examined to discuss the adsorption isotherm and the experimental data were correlated with the Temkin isotherm model.

Declaration of competing interest

The authors declare that they have no known competing financial interests or personal relationships that could have appeared to influence the work reported in this paper.

Acknowledgments

This work was performed in the Advanced Nanomaterials Research Lab and Specialized Materials Science Lab at Beirut Arab University in collaboration with Alexandria University.

Funding

This research did not receive any specific grant from funding agencies in the public, commercial, or not-for-profit sectors.

References

Abdel Maksoud, M.I.A., El-Ghandour, A., Ashour, A.H., Atta, M.M., Abdelhaleem, S., El-Hanbaly, A.H., Fahim, R.A., Kassem, S.M., Shalaby, M.S., Awed, A.S., 2021. La3+ doped LiCo0.25Zn0.25Fe2O4 spinel ferrite nanocrystals: Insights on structural, optical and magnetic properties. J. Rare Earths 39 (1), 75–82. https://doi.org/10.1016/j.jre.2019.12.017.

Ahmad, I., Aslam, M., Jabeen, U., Zafar, M.N., Malghani, M.N.K., Alwadai, N., Alshammari, F.H., Almuslem, A.S., Ullah, Z., 2022. ZnO and Ni-doped ZnO photocatalysts: Synthesis, characterization and improved visible light driven photocatalytic degradation of methylene blue. Inorg. Chim. Acta 543, 121167. https://doi.org/10.1016/j.ica.2022.121167.

Ahmed, M.A., Bishay, S.T., Khafagy, R.M., Saleh, N.M., 2014. Promising wastewater treatment using rare earth-doped nanoferrites. J. Magn. Magn. Mater. 350, 73–80. https://doi.org/10.1016/j.jmmm.2013.09.017.

Akhlaghi, N., Najafpour-Darzi, G., 2021. Manganese ferrite (MnFe2O4) Nanoparticles: From synthesis to application -A review. J. Ind. Eng. Chem. 103, 292–304. https://doi.org/10.1016/j.jiec.2021.07.043.

Ali, I., Peng, C., Ye, T., Naz, I., 2018. Sorption of cationic malachite green dye on phytogenic magnetic nanoparticles functionalized by 3-marcaptopropanic acid. RSC Adv. 8 (16), 8878–8897. https://doi.org/10.1039/C8RA00245B.

Aljohani, M.M., Al-Qahtani, S.D., Alshareef, M., El-Desouky, M.G., El-Bindary, A.A., El-Metwaly, N.M., El-Bindary, M.A., 2023. Highly efficient adsorption and removal bio-staining dye from industrial wastewater onto mesoporous Ag-MOFs. Process Saf. Environ. Prot. 172, 395–407. https://doi.org/10.1016/j.psep.2023.02.036.

Almahri, A., Abou-Melha, K.S., Katouah, H.A., Al-bonayan, A.M., Saad, F.A., El-Desouky, M.G., El-Bindary, A.A., 2023a. Adsorption and removal of the harmful pesticide 2,4-dichlorophenylacetic acid from an aqueous environment via coffee waste biochar: Synthesis, characterization, adsorption study and optimization via Box-Behnken design. J. Mol. Struct. 1293, 136238 https://doi.org/10.1016/j.molstruc.2023.136238.

Almahri, A., Morad, M., Aljohani, M.M., Alatawi, N.M., Saad, F.A., Abumelha, H.M., El-Desouky, M.G., El-Bindary, A.A., 2023b. Atrazine reclamation from an aqueous environment using a ruthenium-based metal-organic framework. Process Saf. Environ. Prot. 177, 52–68. https://doi.org/10.1016/j.psep.2023.06.091.

Alrefaee, S.H., Aljohani, M., Alkhamis, K., Shaaban, F., El-Desouky, M.G., El-Bindary, A. A., El-Bindary, M.A., 2023. Adsorption and effective removal of organophosphorus pesticides from aqueous solution via novel metal-organic framework: Adsorption isotherms, kinetics, and optimization via Box-Behnken design. J. Mol. Liq. 384, 122206 https://doi.org/10.1016/j.molliq.2023.122206.

An, S., Liu, X., Yang, L., Zhang, L., 2015. Enhancement removal of crystal violet dye using magnetic calcium ferrite nanoparticle: Study in single- and binary-solute systems. Chem. Eng. Res. Des. 94, 726–735. https://doi.org/10.1016/j.cherd.2014.10.013.

Ansari, M.R., Kem, A., Agrohi, P., Mallick, P.K., Rao, P., Peta, K.R., 2023. Structural, optical, magnetic and anti-bacterial properties of green synthesized spinel zinc ferrite by microwave-assisted method. Mater. Chem. Phys. 301, 127641 https://doi.org/10.1016/j.matchemphys.2023.127641.

Aridi, A., Awad, R., Khalaf, A., 2021. Synthesis and characterization of ZnFe2O4/Mn2O3 nanocomposites. Appl. Phys. A 127 (3), 206. https://doi.org/10.1007/s00339-021-04362-7.

Aridi, A., Basma, H., Chehade, W., Sayed Hassan, R., Yaacoub, N., Naoufal, D., Awad, R., 2023a. Enhanced adsorption performance of magnetic Ni0.5Zn0.5Fe2O4/Zn0.95Co0.05O nanocomposites for the removal of malachite green dye. In: Environmental Science and Pollution Research. https://doi.org/10.1007/s11356-023-26608-y.

Aridi, A., Naoufal, D., El-Rassy, H., Awad, R., 2023b. Preparation and Characterization of ZnFe2O4/Mn2O3 Nanocatalysts for the Degradation of Nitrobenzene. Chem. Afr. 1–14.

Bagi Aljewaw, O., Karim, M.K.A., Mohamed Kamari, H., Mohd Zaid, M.H., Mohd Noor, N., Che Isa, I.N., Abu Mhareb, M.H., 2020. Impact of Dy2O3 Substitution on the Physical, Structural and Optical Properties of Lithium–Aluminium–Borate Glass System. Appl. Sci. 10 (22), Article 22. https://doi.org/10.3390/app10228183.

Bajorek, A., Berger, C., Dulski, M., Łopadczak, P., Zubko, M., Prusik, K., Wojtyniak, M., Chrobak, A., Grasset, F., Randrianantoandro, N., 2019. Microstructural and magnetic characterization of Ni0.5Zn0.5Fe2O4 ferrite nanoparticles. J. Phys. Chem. Solid 129, 1–21. https://doi.org/10.1016/j.jpcs.2018.12.045.

Bashir, M., Batool, M., Arif, N., Tayyab, M., Zeng, Y.-J., Nadeem Zafar, M., 2023. Strontium-based nanomaterials for the removal of organic/inorganic contaminants from water: A review. Coord. Chem. Rev. 492, 215286 https://doi.org/10.1016/j.ccr.2023.215286.

Basma, H., Al Boukhari, J., Abd Al Nabi, M., Aridi, A., Sayed Hassan, R., Naoufal, D., Roumie, M., & Awad, R. (2022). Enhancement of the magnetic and optical properties of Ni0.5Zn0.5Fe2O4 nanoparticles by ruthenium doping. *Applied Physics A*, *128*(5), 409. https://doi.org/10.1007/s00339-022-05552-7.

Bazrafshan, E., Zarei, A.A., Mohammadi, L., Zafar, M.N., Foroughi, M., Aman, S., Sabri, F., Mahvi, A.H., Barahuie, F., Zafar, M., 2021. Efficient tetracycline removal from aqueous solutions using ionic liquid modified magnetic activated carbon (IL@mAC). J. Environ. Chem. Eng. 9 (6), 106570 https://doi.org/10.1016/j.jece.2021.106570.

Bazrafshan, E., dahmardeh, Z., Mohammadi, L., NadeemZafar, M., Dargahi, A., & Pirdadeh, F. (2023). Synthesis of magnesium oxide nanoparticles and its application for photocatalytic removal of furfural from aqueous media: Optimization using response surface methodology. *Arabian Journal of Chemistry*, *16*(8), 104998. https://doi.org/10.1016/j.arabjc.2023.104998.

Bhalla, N., Taneja, S., Thakur, P., Sharma, P.K., Mariotti, D., Maddi, C., Ivanova, O., Petrov, D., Sukhachev, A., Edelman, I.S., Thakur, A., 2021. Doping Independent Work Function and Stable Band Gap of Spinel Ferrites with Tunable Plasmonic and Magnetic Properties. Nano Lett. 21 (22), 9780–9788. https://doi.org/10.1021/acs.nanolett.1c03767.

Chauhan, A.K., Kataria, N., Garg, V.K., 2020. Green fabrication of ZnO nanoparticles using Eucalyptus spp. Leaves extract and their application in wastewater remediation. Chemosphere 247, 125803. https://doi.org/10.1016/j.chemosphere.2019.125803.

Chehade, W., Basma, H., Abdallah, A. M., Hassan, R. S., & Awad, R. (2022). Synthesis and magneto-optical studies of novel Ni0. 5Zn0. 5Fe2O4/Zn0. 95Co0. 05O nanocomposite as a candidate for photocatalytic applications. *Ceramics International*, *48*(1), 1238–1255.

Chellab, R.M., Harbbi, K.H., 2019. The correction of the line profiles for x-ray diffraction peaks by using three analysis methods. AIP Conf. Proc. 2123 (1), 020044 https://doi.org/10.1063/1.5116971.

Debnath, S., Das, R., 2020. Study of the optical properties of Zn doped Mn spinel ferrite nanocrystals shows multiple emission peaks in the visible range –a promising soft ferrite nanomaterial for deep blue LED. J. Mol. Struct. 1199, 127044 https://doi.org/10.1016/j.molstruc.2019.127044.

Douafer, S., Lahmar, H., Laouici, R., Akika, F.Z., Trari, M., Avramova, I., Benamira, M., 2023. Synthesis and characterization of CdFe2O4 nanoparticles: Application for the removal of Methyl Green under solar irradiation. Mater. Today Commun. 35, 105630 https://doi.org/10.1016/j.mtcomm.2023.105630.

M. El-Metwaly, N., A. Katouah, H., El-Desouky, M. G., El-Bindary, A. A., & El-Bindary, M. A. (2022). Fabricating of Fe_3O_4 @Ag-MOF nanocomposite and evaluating its adsorption activity for removal of doxorubicin. *Journal of Environmental Science and Health, Part A*, *57*(13–14), 1099–1115. https://doi.org/10.1080/10934529.2022.2156230.

Etemadinia, T., Barikbin, B., Allahresani, A., 2019. Removal of congo red dye from aqueous solutions using znfe2o4/sio2/Tragacanth gum magnetic nanocomposite as a novel adsorbent. Surf. Interfaces 14, 117–126. https://doi.org/10.1016/j.surfin.2018.10.010.

Eyvazi, B., Jamshidi-Zanjani, A., Darban, A.K., 2020. Synthesis of nano-magnetic MnFe2O4 to remove Cr(III) and Cr(VI) from aqueous solution: A comprehensive study. Environ. Pollut. 265, 113685 https://doi.org/10.1016/j.envpol.2019.113685.

Fathy, M.A., Kamel, A.H., Hassan, S.S., 2022. Novel magnetic nickel ferrite nanoparticles modified with poly (aniline-co-o-toluidine) for the removal of hazardous 2, 4-dichlorophenol pollutant from aqueous solutions. RSC Advances 12 (12), 7433–7445.

Fernández, A., Araujo, F.P., Guerra, Y., Castro-Lopes, S., Matilla-Arias, J., de Lima, I.S., Silva-Filho, E.C., Osajima, J.A., Guerrero, F., Peña-Garcia, R., 2023. Synthesis of coral-like structures of Pr–Yb co-doped YIG: Structural, optical, magnetic and antimicrobial properties. J. Rare Earths. https://doi.org/10.1016/j.jre.2023.03.006.

Ghamkhari, A., Mohamadi, L., Kazemzadeh, S., Zafar, M.N., Rahdar, A., Khaksefidi, R., 2020. Synthesis and characterization of poly(styrene-block-acrylic acid) diblock copolymer modified magnetite nanocomposite for efficient removal of penicillin G. Compos. B Eng. 182, 107643 https://doi.org/10.1016/j.compositesb.2019.107643.

Hammad, A.B., 2022. Development of dielectric and magnetic properties of advanced nano-engineering composites. Egypt. J. Chem. 65 (11), 141–154. https://doi.org/10.21608/ejchem.2022.114030.5184.

Hassan, N., Shahat, A., El-Didamony, A., El-Desouky, M.G., El-Bindary, A.A., 2020. Synthesis and characterization of ZnO nanoparticles via zeolitic imidazolate framework-8 and its application for removal of dyes. J. Mol. Struct. 1210, 128029 https://doi.org/10.1016/j.molstruc.2020.128029.

Keerthana, S.P., Yuvakkumar, R., Kumar, P.S., Ravi, G., Velauthapillai, D., 2021. Rare earth metal (Sm) doped zinc ferrite (ZnFe2O4) for improved photocatalytic elimination of toxic dye from aquatic system. Environ. Res. 197, 111047 https://doi.org/10.1016/j.envres.2021.111047.

Kefeni, K.K., Mamba, B.B., 2020. Photocatalytic application of spinel ferrite nanoparticles and nanocomposites in wastewater treatment: Review. Sustain. Mater. Technol. 23, e00140.

Kefeni, K.K., Msagati, T.A.M., Nkambule, T.T.I., Mamba, B.B., 2020. Spinel ferrite nanoparticles and nanocomposites for biomedical applications and their toxicity. Mater. Sci. Eng. C 107, 110314. https://doi.org/10.1016/j.msec.2019.110314.

Konicki, W., Sibera, D., Mijowska, E., Lendzion-Bieluń, Z., Narkiewicz, U., 2013. Equilibrium and kinetic studies on acid dye Acid Red 88 adsorption by magnetic ZnFe2O4 spinel ferrite nanoparticles. J. Colloid Interface Sci. 398, 152–160. https://doi.org/10.1016/j.jcis.2013.02.021.

Köseoğlu, Y., 2015. Structural and magnetic properties of Cr doped NiZn-ferrite nanoparticles prepared by surfactant assisted hydrothermal technique. Ceram. Int. 41 (5, Part A), 6417–6423. https://doi.org/10.1016/j.ceramint.2015.01.079.

Kumar, G., Shah, J., Kotnala, R. K., Singh, V. P., Sarveena, Garg, G., Shirsath, S. E., Batoo, K. M., & Singh, M. (2015). Superparamagnetic behaviour and evidence of weakening in super-exchange interactions with the substitution of Gd3+ ions in the Mg–Mn nanoferrite matrix. *Materials Research Bulletin*, *63*, 216–225. https://doi.org/10.1016/j.materresbull.2014.12.009.

Kumar, A., Gora, M.K., Lal, G., Choudhary, B.L., Meena, P.L., Dhaka, R.S., Singhal, R.K., Kumar, S., Dolia, S.N., 2023. Impact of Gd3+ doping on structural, electronic, magnetic, and photocatalytic properties of MnFe2O4 nanoferrites and application in dye-polluted wastewater remediation. Environ. Sci. Pollut. Res. 30 (7), 18820–18842. https://doi.org/10.1007/s11356-022-23420-y.

Lafi, R., Montasser, I., Hafiane, A., 2019. Adsorption of congo red dye from aqueous solutions by prepared activated carbon with oxygen-containing functional groups and its regeneration. Adsorpt. Sci. Technol. 37 (1–2), 160–181. https://doi.org/10.1177/0263617418819227.

Lemziouka, H., Boutahar, A., Moubah, R., Omari, L.H., Bahhar, S., Abid, M., Lassri, H., 2020. Synthesis, structural, optical and dispersion parameters of La-doped spinel zinc ferrites ZnFe2-xLaxO4 (x = 0.00, 0.001, 0.005, 0.01 and 0.015). Vacuum 182, 109780. https://doi.org/10.1016/j.vacuum.2020.109780.

Li, Y., Wang, T., Zhang, S., Zhang, Y., Yu, L., Liu, R., 2021. Adsorption and electrochemical behavior investigation of methyl blue onto magnetic nickel-magnesium ferrites prepared via the rapid combustion process. J. Alloys Compounds 885, 160969. https://doi.org/10.1016/j.jallcom.2021.160969.

Liu, X., An, S., Wang, Y., Yang, Q., Zhang, L., 2015. Rapid selective separation and recovery of a specific target dye from mixture consisted of different dyes by magnetic Ca-ferrites nanoparticles. Chem. Eng. J. 262, 517–526. https://doi.org/10.1016/j.cej.2014.10.002.

Liu, S., Ouyang, H., Wang, Z., 2022. Combustion process for magnetic copper–cobalt ferrite and its Congo red adsorption property. Mater. Res. Express 9 (7), 075003. https://doi.org/10.1088/2053-1591/ac7f82.

Luo, T., Hou, X., Liang, Q., Zhang, G., Chen, F., Xia, Y., Ru, Q., Yao, L., Wu, Y., 2018. The influence of manganese ions doping on nanosheet assembly NiFe2O4 for the removal of Congo red. J. Alloy. Compd. 763, 771–780. https://doi.org/10.1016/j.jallcom.2018.05.203.

Manikandan, V., Kuncser, V., Vasile, B., Kavita, S., Vigneselvan, S., Mane, R.S., 2019. Enhancement in magnetic and dielectric properties of the ruthenium-doped copper ferrite(Ru-CuFe2O4) nanoparticles. J. Magnet. Magnet. Mater. 476, 18–23. https://doi.org/10.1016/j.jmmm.2018.12.050.

Mathew, D.S., Juang, R.-S., 2007. An overview of the structure and magnetism of spinel ferrite nanoparticles and their synthesis in microemulsions. Chem. Eng. J. 129 (1), 51–65. https://doi.org/10.1016/j.cej.2006.11.001.

Mishra, S., Sahoo, S.S., Debnath, A.K., Muthe, K.P., Das, N., Parhi, P., 2020. Cobalt ferrite nanoparticles prepared by microwave hydrothermal synthesis and adsorption efficiency for organic dyes: Isotherms, thermodynamics and kinetic studies. Adv. Powder Technol. 31 (11), 4552–4562. https://doi.org/10.1016/j.apt.2020.10.001.

Mohammadi, L., Zafar, M.N., Bashir, M., Sumra, S.H., Shafqat, S.S., Zarei, A.A., Dahmardeh, H., Ahmad, I., Halawa, M.I., 2021. Modeling of phenol removal from water by NiFe2O4 nanocomposite using response surface methodology and artificial neural network techniques. J. Environ. Chem. Eng. 9 (4), 105576 https://doi.org/10.1016/j.jece.2021.105576.

Muedi, K. L., Masindi, V., Maree, J. P., Haneklaus, N., & Brink, H. G. (2022). Effective Adsorption of Congo Red from Aqueous Solution Using Fe/Al Di-Metal Nanostructured Composite Synthesised from Fe(III) and Al(III) Recovered from Real Acid Mine Drainage. *Nanomaterials*, *12*(5), Article 5. https://doi.org/10.3390/nano12050776.

Panda, S.K., Aggarwal, I., Kumar, H., Prasad, L., Kumar, A., Sharma, A., Vo, D.-V.-N., Van Thuan, D., Mishra, V., 2021. Magnetite nanoparticles as sorbents for dye removal: A review. Environ. Chem. Lett. 19 (3), 2487–2525. https://doi.org/10.1007/s10311-020-01173-9.

Patade, S.R., Andhare, D.D., Kharat, P.B., Humbe, A.V., Jadhav, K.M., 2020. Impact of crystallites on enhancement of bandgap of Mn1-xZnxFe2O4 (1 ≥ x ≥ 0) nanospinels. Chem. Phys. Lett. 745, 137240 https://doi.org/10.1016/j.cplett.2020.137240.

Patil, A. D., Patange, S. M., Dighe, P. M., Shaikh, S. F., Rana, A. ul H. S., Pandit, B., & Jadhav, S. S. (2022). Tuning the structural, optical and magnetic properties of NiCuZn (Ni0.4Cu0.3Zn0.3Fe2O4) spinel ferrites by Nb2O5 additive. *Ceramics International*. https://doi.org/10.1016/j.ceramint.2022.06.016.

Pham, V.T., Nguyen, H.-T.-T., Tran, T.V., Nguyen, D.T.C., Le, H.T.N., Nguyen, T.T., Vo, D.-V.-N., Le, T.H.N., Nguyen, D.C., 2019. Kinetics, Isotherm, Thermodynamics, and Recyclability of Exfoliated Graphene-Decorated MnFe $_{2\ O}$ 4 Nanocomposite Towards Congo Red Dye. J. Chem. 2019, 1–16. https://doi.org/10.1155/2019/5234585.

Phan, H.T., Haes, A.J., 2019. What Does Nanoparticle Stability Mean? J. Phys. Chem. C 123 (27), 16495–16507. https://doi.org/10.1021/acs.jpcc.9b00913.

Pooladi, M., Shokrollahi, H., Lavasani, S.A.N.H., Yang, H., 2019. Investigation of the structural, magnetic and dielectric properties of Mn-doped Bi2Fe4O9 produced by reverse chemical co-precipitation. Mater. Chem. Phys. 229, 39–48. https://doi.org/10.1016/j.matchemphys.2019.02.076.

Roman, T., Asavei, R.-L., Karkalos, N.E., Roman, C., Virlan, C., Cimpoesu, N., Istrate, B., Zaharia, M., Markopoulos, A.P., Kordatos, K., Stanciu, S., Pui, A., 2019. Synthesis and adsorption properties of nanocrystalline ferrites for kinetic modeling development. Int. J. Appl. Ceram. Technol. 16 (2), 693–705. https://doi.org/10.1111/ijac.13091.

Sachin, J., Singh, N., Singh, R., Shah, K., Pramanik, B.K., 2023. Green synthesis of zinc oxide nanoparticles using lychee peel and its application in anti-bacterial properties and CR dye removal from wastewater. Chemosphere 327, 138497. https://doi.org/10.1016/j.chemosphere.2023.138497.

Samoila, P., Cojocaru, C., Cretescu, I., Stan, C.D., Nica, V., Sacarescu, L., Harabagiu, V., 2015. Nanosized spinel ferrites synthesized by sol-gel autocombustion for optimized removal of azo dye from aqueous solution. J. Nanomater. 16 (1), 237:237. https://doi.org/10.1155/2015/713802.

Sandeep, Y., Rambabu, T., Kunja, L., Borang, O., Aravind, G., Dode, A., Nathanial, V., 2022. Low sintering effect on structural, electrical and magnetic properties of rare-earth metal ion Er3+-substituted nickel–zinc spinal ferrites. J. Mater. Sci. Mater. Electron. 33 (2), 635–651. https://doi.org/10.1007/s10854-021-07332-0.

Sarveena. (2021). Chapter 11—Structural and Magnetic Properties of Ni Nanoferrites Doped With Rare Earth and Transition Metals. In G. K. Bhargava, S. Bhardwaj, M. Singh, & K. M. Batoo (Eds.), *Ferrites and Multiferroics: Fundamentals to Applications* (pp. 91–106). Springer. https://doi.org/10.1007/978-981-16-7454-9_5.

Sattar, A., Bofeng, B., Khalil, M., Sajjad, M., 2022. Detailed analysis of structural, optical and photo catalytic properties of spinel nickel doped magnesium zinc ferrites at different substitutions. Inorg. Chem. Commun. 142, 109505 https://doi.org/10.1016/j.inoche.2022.109505.

Seyring, M., Song, X., Chuvilin, A., Kaiser, U., Rettenmayr, M., 2009. Characterization of grain structure in nanocrystalline gadolinium by high-resolution transmission electron microscopy. J. Materi. Res. 24 https://doi.org/10.1557/jmr.2009.0071.

Simonescu, C.M., Tătăruş, A., Culiţă, D.C., Stănică, N., Butoi, B., Kuncser, A., 2021a. Facile Synthesis of Cobalt Ferrite (CoFe2O4) Nanoparticles in the Presence of Sodium Bis (2-ethyl-hexyl) Sulfosuccinate and Their Application in Dyes Removal from Single and Binary Aqueous Solutions. Nanomaterials 11 (11), Article 11. https://doi.org/10.3390/nano11113128.

Simonescu, C.M., Tătăruş, A., Culiţă, D.C., Stănică, N., Ionescu, I.A., Butoi, B., Banici, A.-M., 2021b. Comparative Study of CoFe2O4 Nanoparticles and CoFe2O4-Chitosan Composite for Congo Red and Methyl Orange Removal by Adsorption. Nanomaterials 11 (3), 711. https://doi.org/10.3390/nano11030711.

Singh, J.P., Srivastava, R.C., Agrawal, H.M., 2010. Optical Behaviour of Zinc Ferrite Nanoparticles. AIP Conf. Proc. 1276 (1), 137–143. https://doi.org/10.1063/1.3504278.

Singh Yadav, R., Kuřitka, I., Havlica, J., Hnatko, M., Alexander, C., Masilko, J., Kalina, L., Hajdúchová, M., Rusnak, J., Enev, V., 2018. Structural, magnetic, elastic, dielectric and electrical properties of hot-press sintered Co1−xZnxFe2O4 (x=0.0, 0.5) spinel ferrite nanoparticles. J. Magnet. Magnet. Mater. 447, 48–57. https://doi.org/10.1016/j.jmmm.2017.09.033.

Subbaiah Munagapati, V., Wen, H.-Y., Gollakota, A.R.K., Wen, J.-C., Shu, C.-M., Andrew Lin, K.-Y., Tian, Z., Wen, J.-H., Mallikarjuna Reddy, G., Zyryanov, G.V., 2022. Magnetic Fe3O4 nanoparticles loaded papaya (Carica papaya L.) seed powder as an effective and recyclable adsorbent material for the separation of anionic azo dye (Congo Red) from liquid phase: Evaluation of adsorption properties. J. Mole. Liq. 345, 118255 https://doi.org/10.1016/j.molliq.2021.118255.

Suresh, J., Babu, B.V., Krishna, A.R., Reddy, P.V.S.S.S.N., Trinadh, B., Mohan, B.S., Rao, K.E., Samatha, K., 2022. Structural, electrical and magnetic studies of Ni0.7Mn0.2Cu0.1Fe2-xAlxO4 (x = 0, 0.05, 0.1, 0.15, 0.2 and 0.25) nano-ferrite synthesized by sol-gel technique. Chin. J. Phys. 80, 334–348. https://doi.org/10.1016/j.cjph.2022.06.005.

Tan, L.V., Thinh, P.V., Tham, N.T.H., Sy, D.T., 2020. Kinetic and Isotherm Modelling of the Adsorption of Congo Red Dye onto NiFe2O4 and NiFe2O4 decorated Exfoliated Graphite. IOP Conf. Ser.: Mater. Sci. Eng. 991 (1), 012085 https://doi.org/10.1088/1757-899X/991/1/012085.

Taneja, S., Thakur, P., Kumar, R., Hemalatha, S., Slimani, Y., Ravelo, B., & Thakur, A. (2022). Nanostructured Rare Earth Nd3+doped Nickel–Zinc–Bismuth Spinel Ferrites: Structural, Electrical and Dielectric Studies. *Ceramics International*, *48*(19, Part A), 27731–27738. https://doi.org/10.1016/j.ceramint.2022.06.073.

Thakur, P., Sharma, R., Kumar, M., Katyal, S.C., Negi, N.S., Thakur, N., Sharma, V., Sharma, P., 2016. Superparamagnetic La doped Mn–Zn nano ferrites: Dependence on dopant content and crystallite size. Mater. Res. Express 3 (7), 075001. https://doi.org/10.1088/2053-1591/3/7/075001.

Vinod, G., Rajashekhar, K., Naik, J.L., 2022. Dysprosium doped Cu0.8Cd0.2DyxFe2-xO4 nano ferrites: A combined impact of Dy3+ on enhanced physical, optical, magnetic, and DC-electrical properties. Ceram. Int. https://doi.org/10.1016/j.ceramint.2022.09.265.

Vodă, R., Lupa, L., Negrea, A., Ciopec, M., Negrea, P., Davidescu, C.M., 2016. The development of a new efficient adsorbent for the removal of methylene blue. Sep. Sci. Technol. 51 (15–16), 2511–2518. https://doi.org/10.1080/01496395.2016.1171238.

Wekoye, J.N., Wanyonyi, W.C., Wangila, P.T., Tonui, M.K., 2020. Kinetic and equilibrium studies of Congo red dye adsorption on cabbage waste powder. Environ. Chem. Ecotoxicol. 2, 24–31. https://doi.org/10.1016/j.enceco.2020.01.004.

Wu, R., Qu, J., 2005. Removal of water-soluble azo dye by the magnetic material MnFe2O4. J. Chem. Technol. Biotechnol. 80 (1), 20–27. https://doi.org/10.1002/jctb.1142.

Yang, L., Zhang, Y., Liu, X., Jiang, X., Zhang, Z., Zhang, T., Zhang, L., 2014. The investigation of synergistic and competitive interaction between dye Congo red and methyl blue on magnetic MnFe2O4. Chem. Eng. J. 246, 88–96. https://doi.org/10.1016/j.cej.2014.02.044.

Zafar, B., Shafqat, S.S., Zafar, M.N., Haider, S., Sumrra, S.H., Zubair, M., Alwadai, N., Alshammari, F.H., Almuslem, A.S., Akhtar, M.S., 2022. NaHCO3 assisted multifunctional Co3O4, CuO and Mn2O3 nanoparticles for tartrazine removal from synthetic wastewater and biological activities. Mater. Today Commun. 33, 104946 https://doi.org/10.1016/j.mtcomm.2022.104946.

Zeng, S., Duan, S., Tang, R., Li, L., Liu, C., Sun, D., 2014. Magnetically separable Ni0.6Fe2.4O4 nanoparticles as an effective adsorbent for dye removal: Synthesis and study on the kinetic and thermodynamic behaviors for dye adsorption. Chem. Eng. J. 258, 218–228. https://doi.org/10.1016/j.cej.2014.07.093.

Zhou, X., Zhou, Y., Zhou, L., Wei, J., Wu, J., Yao, D., 2019. Effect of Gd and La doping on the structure, optical and magnetic properties of NiZnCo ferrites. Ceram. Int. 45 (5), 6236–6242. https://doi.org/10.1016/j.ceramint.2018.12.102.